

The Unreasonable Effectiveness of Guidance for Diffusion Models

Tim Kaiser*

Heinrich Heine University of Dusseldorf
tikai103@hhu.de

Nikolas Adaloglou*

Heinrich Heine University of Dusseldorf
adaloglo@hhu.de

Markus Kollmann

Heinrich Heine University of Dusseldorf
markus.kollmann@hhu.de

Abstract

Guidance is an error-correcting technique used to improve the perceptual quality of images generated by diffusion models. Typically, the correction is achieved by linear extrapolation, using an auxiliary diffusion model that has lower performance than the primary model. Using a 2D toy example, we show that it is highly beneficial when the auxiliary model exhibits similar errors as the primary one but stronger. We verify this finding in higher dimensions, where we show that competitive generative performance to state-of-the-art guidance methods can be achieved when the auxiliary model differs from the primary one only by having stronger weight regularization. As an independent contribution, we investigate whether upweighting long-range spatial dependencies improves visual fidelity. The result is a novel guidance method, which we call sliding window guidance (SWG), that guides the primary model with itself by constraining its receptive field. Intriguingly, SWG aligns better with human preferences than state-of-the-art guidance methods while requiring neither training, architectural modifications, nor class conditioning. The code will be released.

1. Introduction

Diffusion models (DMs) have emerged as a powerful approach for generative tasks, achieving remarkable success in areas such as image synthesis and text-to-image generation [1, 17, 24, 27, 41, 44, 45]. DMs are a class of generative models that iteratively transform noise samples into samples that are close to a desired data distribution. Despite their success, DMs often fail to generate high-quality samples in the visual domain [3] and require guidance techniques to improve visual fidelity (Fig. 1). The current most



Figure 1. **Left:** Even state-of-the-art diffusion models can fail to generate globally coherent images without guidance. **Right:** Sliding window guidance (SWG) upweights long-range dependencies and thereby improves global coherence on average.

popular method, classifier-free guidance (CFG), improves image quality by increasing the probability that an image belongs to a certain class label [25]. Unlike its predecessor, classifier guidance [12], which relies on training an external classifier on labeled noisy images, CFG combines conditional and unconditional denoisers, which can be trained jointly [16].

In the following, we denote by \mathbf{x} a noisy image and by $\epsilon(\mathbf{x}, t; c)$ and $\epsilon(\mathbf{x}, t)$ the class conditional and unconditional noise predictors at timestep t of the denoising process [12]. CFG linearly combines noise predictions during sampling using the extrapolation scheme

$$\tilde{\epsilon}(\mathbf{x}, t; c) = \epsilon(\mathbf{x}, t; c) + w[\epsilon(\mathbf{x}, t; c) - \epsilon(\mathbf{x}, t)], \quad (1)$$

with guidance weight $w > 0$. CFG can be viewed as an error-correcting method [7, 45]. Equivalent extrapolation schemes can be found for all diffusion model formulations, such as target prediction [24] or flow matching [42].

Despite the widespread use of CFG in conditional synthesis [37], it comes with notable limitations. First, it increases the training budget: when trained jointly, the unconditional task can consume up to 20% of the computational

*The authors contributed equally. Random order.

cost [16]. Additionally, while CFG reduces class mismatch between samples and condition c of the noise predictor [41], this benefit comes at the expense of sample diversity, as this sampling method focuses on regions with high class probability [25]. Since guidance is a linear extrapolation scheme, the sampling trajectory can overshoot the desired distribution, leading to highly simplified images [30]. Finally, CFG sampling is restricted to class conditional generation by design.

Recently, a new class of guidance methods has been developed that address some of the limitations of CFG. These methods utilize the extrapolation scheme of Eq. (1) in a more generic way

$$\tilde{\epsilon}(\mathbf{x}, t) = \epsilon_{\text{pos}}(\mathbf{x}, t) + w[\epsilon_{\text{pos}}(\mathbf{x}, t) - \epsilon_{\text{neg}}(\mathbf{x}, t)], \quad (2)$$

where the subscripts pos for positive and neg for negative simply refer to the sign of the noise predictors. We consider ϵ_{pos} to be a trained, well-performing DM. The idea behind Eq. (2) is to extrapolate into high likelihood regions by designing a negative model that has an inferior performance compared to ϵ_{pos} .

Typically, ϵ_{neg} is derived from ϵ_{pos} by re-training using fewer parameters, architecture-based heuristic manipulations, or shorter training times [2, 25]. We refer to this class of guidance methods as *weak model guidance (WMG)*. While WMG methods seem promising, they often require training additional models, heavy model-specific hyperparameter tuning at sampling time [25], or manual selection of specific layers to impair [2].

In this paper, we first introduce a 2D toy example to show that (i) WMG samples closer to high likelihood regions than CFG and (ii) guidance works best if ϵ_{neg} makes similar errors as ϵ_{pos} but stronger. Assuming that the generative error of ϵ_{pos} can be primarily attributed to scaling factors, such as training time and number of parameters [22], further constraining these factors allows us to construct ϵ_{neg} in a principled way. To this end, we show that constructing ϵ_{neg} by re-training or fine-tuning ϵ_{pos} under increased weight regularization results in competitive performance compared to state-of-the-art guidance methods. Additionally, to improve perceptual image quality, we introduce sliding window guidance (SWG), a novel guidance method designed to upweight long-range dependencies (Fig. 1). In contrast to existing guidance techniques [2, 16, 25, 30, 39, 41, 48], SWG requires neither training, architectural modifications nor class conditioning and can be applied to any DM that can process multiple image resolutions. Finally, SWG achieves competitive generative performance while aligning better with human preferences than state-of-the-art techniques.

2. Related work

Classifier-free guidance (CFG) requires an unconditional denoiser, which can be trained jointly using dropout or separately. CFG-based sampling can be improved by adding a noise schedule to the condition [39], introducing monotonically increasing guidance weight schedules [48], step-wise intensity thresholding [41], or applying CFG only at an interval in the intermediate denoising steps [30]. Despite recent advancements, CFG cannot be applied to unlabelled datasets or conditional-only trained denoisers by design. While several sampling methods focus on modifying CFG [30, 39, 41, 48], alternative guidance techniques that do not require additional training or fine-tuning and can be applied to both conditional and unconditional sampling remain an open quest [40].

Alternative guidance methods can be roughly grouped into three categories: i) *architecture-based impairments*, ii) *image-level manipulations* [19], and iii) inferior capacity models, which we refer to as *weak models*. Architectural impairments typically leverage self-attention maps [2, 18] that are known to capture structure-related information [2, 6, 14, 33]. For instance, a handful of manually picked attention maps can be replaced with an identity matrix [2] or filtered using Gaussian smoothing [18]. Nonetheless, the choice of attention maps depends on the model architecture and thus limits the applicability of the method. Finally, architecture-specific impairments can create significant side effects such as deteriorating the visual structure [18]. Image-level manipulations such as frequency filtering have been attempted with limited success [19]. Hong et al. [19] restrict the high-frequency filtering on image patches corresponding to high activation areas, achieved by upsampling self-attention maps. However, similar to architecture-based impairments, it requires cherry-picking while being prone to artifacts [18].

Weak models of inferior capacity compared to the positive model can be constructed by limiting the network size (i.e. number of parameters) or its training time [25] or a combination of both. However, such approaches require additional training from scratch or various weight instances, which are not always available. Concurrent work [4] deteriorates the positive model by fine-tuning with its own generated samples to derive the negative model. Similar to [4], we deteriorate the learning capacity of the positive model by fine-tuning with stronger weight regularization.

Our work is related to [4, 25], yet we aim to systematically study WMG methods and highlight that the negative model needs to exhibit *a similar modeling error as the positive model, but stronger*. While the latter statement is implicitly ingrained in the design choices of prior works [2, 19, 25], it has not been explicitly formulated.

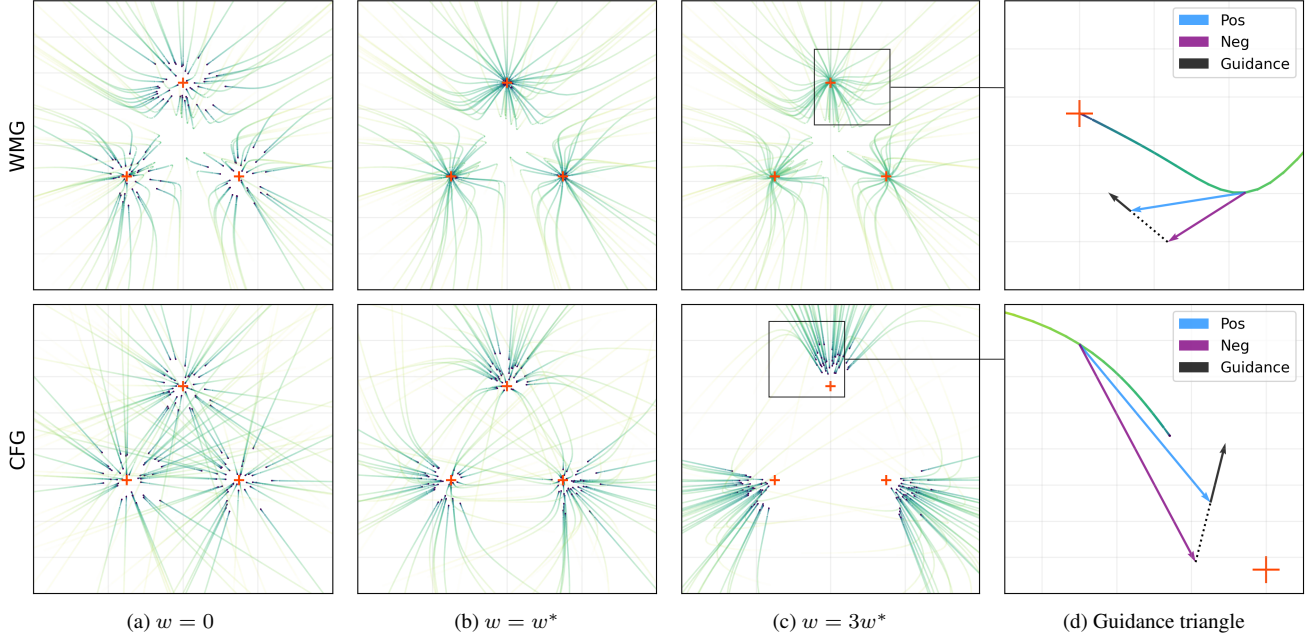


Figure 2. Inference trajectories for our 2D-toy model. (a) $w = 0$ yields the trajectories of the positive model. (b) w^* denotes the guidance weight that leads to best (CFG) or onset of saturating (WMG) performance ($w^* = 1$ for CFG and $w^* = 5$ for WMG). (c) Extreme guidance weights can lead to even smaller endpoint errors but eventually to unstable trajectories for WMG and higher endpoint errors for CFG. (d) Single trajectory zoom. The guidance correction (black arrow) pushes WMG closer to the data point but pushes CFG further away.

3. CFG and WMG behave differently

In the following, we introduce a two-dimensional toy example (Figure 2) to visualize the conceptual differences between CFG and WMG. The data distribution of our toy example consists of three data points $\mathcal{D} = \{\mathbf{y}_1, \mathbf{y}_2, \mathbf{y}_3\}$, where each data point is assigned a different class label $c \in \{1, 2, 3\}$. We can generate trajectories $\mathbf{x}(t)$ by numerically solving the ordinary differential equation (ODE) $d\mathbf{x}(t) = \boldsymbol{\epsilon}^*(\mathbf{x}(t), t)d\sigma(t)$, with $\boldsymbol{\epsilon}^*$ the optimal noise predictor in the Bayesian sense (posterior mean), and $\sigma(t) \in [0, \sigma_{max}]$ the current noise level. Note that $d\sigma(t) < 0$ along a denoising trajectory. It can be shown that for a finite set of data points, the optimal noise predictor takes the explicit form $\boldsymbol{\epsilon}^*(\mathbf{x}, t) = \sigma(t)^{-1} \sum_{n=1}^3 (\mathbf{x} - \mathbf{y}_n) p(\mathbf{y}_n | \mathbf{x}, t) d\mathbf{y}$, with $p(\mathbf{y} | \mathbf{x}, t) = \mathcal{N}(\mathbf{x} | \mathbf{y}, \sigma(t)^2) / \sum_{n=1}^3 \mathcal{N}(\mathbf{x} | \mathbf{y}_n, \sigma(t)^2)$ (see appendix of [24]). We write $\boldsymbol{\epsilon}(\mathbf{x}, t) = \boldsymbol{\epsilon}(\mathbf{x}, \sigma(t))$ to indicate that the time dependence enters exclusively through $\sigma(t)$. The optimal noise predictor generates trajectories with endpoints arbitrarily close to one of the data points if the ODE is initialized with $\mathbf{x}_{init} \sim \mathcal{N}(\mathbf{x} | 0, \sigma_{max})$ and σ_{max} is sufficiently large.

Assume we are given an error-prone noise predictor, $\boldsymbol{\epsilon}_{err}$, whose endpoints are distributed as a superposition of three normal distributions, all with variance δ^2 , and each normal distribution centered around a different data point. For this special case it can be shown that $\boldsymbol{\epsilon}_{err}(\mathbf{x}, t) =$

$\sigma(t)^2 / \tilde{\sigma}(t)^2 \boldsymbol{\epsilon}^*(\mathbf{x}, \tilde{\sigma}(t))$, with $\tilde{\sigma}(t)^2 = \sigma(t)^2 + \delta^2$. The question is now, to what extent CFG and WMG can help to shift the trajectory endpoints of the error-prone predictor closer to the data distribution? To answer this question, we introduce the error-prone predictors $\boldsymbol{\epsilon}_{pos}$, $\boldsymbol{\epsilon}_{neg}$ and adjust the guidance weight w of Eq. 2 such that the error between $\tilde{\boldsymbol{\epsilon}}$ and $\boldsymbol{\epsilon}^*$ is minimized. We recover the CFG setting by introducing the class-conditional noise predictor $\boldsymbol{\epsilon}_{pos}(\mathbf{x}, t) = \boldsymbol{\epsilon}_{err}(\mathbf{x}, t; c)$ and the unconditional noise predictor $\boldsymbol{\epsilon}_{neg}(\mathbf{x}, t) = \boldsymbol{\epsilon}_{err}(\mathbf{x}, t)$. Likewise we recover the WMG setting by $\boldsymbol{\epsilon}_{pos}(\mathbf{x}, t) = \boldsymbol{\epsilon}_{err}(\mathbf{x}, t)$ and $\boldsymbol{\epsilon}_{neg}(\mathbf{x}, t) = \boldsymbol{\epsilon}'_{err}(\mathbf{x}, t)$, where $\boldsymbol{\epsilon}'_{err}$ differs from $\boldsymbol{\epsilon}_{err}$ by a stronger endpoint variance $\delta' > \delta$. The denoising trajectories shown in Figure 2 follow from numerically solving the ODE for $\mathbf{x}(t)$, using Eq. 2 instead of the optimal noise predictor.

CFG. As we use just one datapoint per class, the class conditional noise predictor is given by $\boldsymbol{\epsilon}_{pos}(\mathbf{x}, t) = \sigma(t)^{-1}(\mathbf{x} - \mathbf{y}_{i_c})$, with i_c the data point index belonging to class c , resulting in the special case of a straight line as denoising trajectory (Figure 2a, CFG). For small guidance weights, the trajectory endpoints match slightly better to the data distribution (Figure 2b, CFG), but for larger guidance weights, they move away from data distribution (Figure 2c, CFG). This behavior follows from the fact that $\boldsymbol{\epsilon}_{pos}$ drives the trajectory towards the data point with the corresponding class label, whereas $\boldsymbol{\epsilon}_{neg}$ denoises in the direction of a weighted superposition of all data points. As a result, guid-

ance shifts the trajectories away from the center of mass of the data distribution (Figure 2d, CFG). This behavior has been described in previous works [16] and scales to higher dimensions, e.g., images, where a better distribution overlap between generated samples and training samples in feature space can only be observed for sufficiently small guidance weights.

WMG. In contrast to CFG, increasing the guidance weight for WMG drives trajectory endpoints closer to the data distribution (Figure 2a-c, WMG), up to the point where trajectories become unstable. The crucial assumption for WMG to work well is that endpoint errors of ϵ_{neg} must have higher variance than those of ϵ_{pos} in every dimension. Consequently, in each step, the prediction of ϵ_{pos} is closer to ϵ^* than the prediction of ϵ_{neg} , causing the extrapolation to correct the prediction of ϵ_{pos} towards the prediction of ϵ^* (Figure 2d, WMG). For WMG, our toy example considers the special case that ϵ_{pos} and ϵ_{neg} exhibit the same error up to a multiplicative factor, across all dimensions. For this special case, the guidance term allows us to recover the endpoints of ϵ^* by using the optimal guidance weight

$$w^*(\mathbf{x}, t) = \frac{\|\epsilon_{pos}(\mathbf{x}, t) - \epsilon^*(\mathbf{x}, t)\|}{\|\epsilon_{pos}(\mathbf{x}, t) - \epsilon_{neg}(\mathbf{x}, t)\|},$$

which typically increases monotonically along denoising trajectories (see supplementary material). This optimal weight is obviously of little practical use as it requires the optimal noise predictor ϵ^* . However, we observe excellent, albeit not perfect, matching between endpoints and data-points for constant but sufficiently large weights, significantly better than the accumulated error between optimal and guided trajectories would suggest. The findings of our toy example for WMG have been confirmed in higher dimensions, where significant improvements in the generation of natural images have been found for ϵ_{neg} designed to make similar errors as ϵ_{pos} but stronger [25].

4. Diffusion guidance methods

Baselines. We compare against various baseline methods in our experimental analysis, such as vanilla CFG, CFG using a smaller capacity model (CFG[†]), classifier guidance (CG), and the recent training-free self-attention guidance (SAG [19]). Sampling without guidance ($w = 0$) is equivalent to sampling with ϵ_{pos} .

4.1. Weak model guidance (WMG)

Motivated by the toy example, we focus on diffusion guidance methods that implicitly aim to satisfy the “similar error but stronger” condition to construct ϵ_{neg} from ϵ_{pos} . Reducing the compute time and the number of parameters are well-studied ways of bottlenecking model performance [22] and have been utilized in concurrent work [25], unlike in-

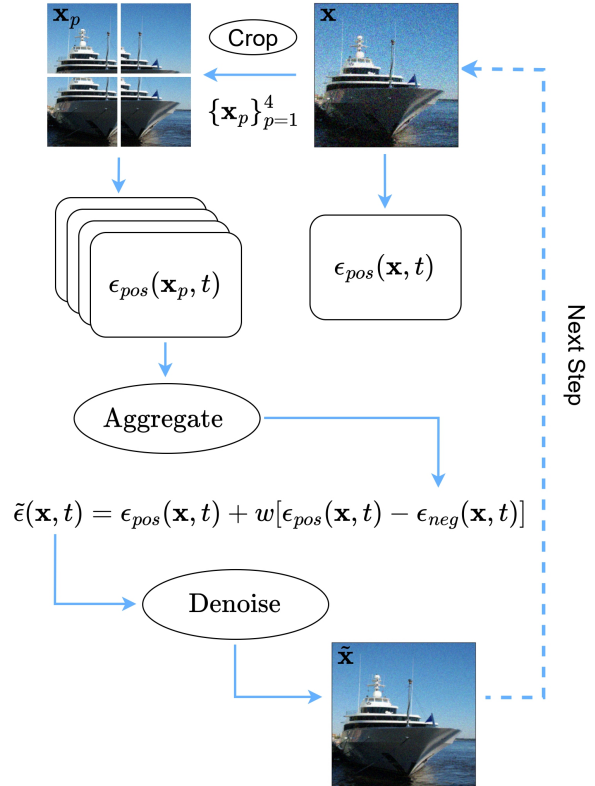


Figure 3. An illustration of sliding window guidance (SWG). We use ϵ_{pos} to independently process $N = 4$ overlapping image crops. ϵ_{neg} is generated by superimposing the processed crops in original order and averaging the overlapping pixels.

creased weight regularization. We realize WMG using the following strategies:

1. **Reduced training** constructs ϵ_{neg} based on parameter instances of ϵ_{pos} from earlier training iterations. This requires access to previous model instances or checkpoints, which are not always publicly available.
2. **Reduced capacity** refers to training a new model on the same task with a smaller model capacity. This is typically achieved by reducing the number of parameters.
3. **Reduced capacity and training (RCT)** combines the above two strategies. Concurrent work [25] recently coined this approach as *autoguidance*. The authors demonstrate a nuanced interconnection between sampling-related hyperparameters that are specific to the EDM2 model [26]. Specifically, the impact of the post-training exponential moving averages (EMAs) used for the positive and negative models, which requires tuning five hyperparameters simultaneously. To make our analysis more generally applicable, we instead set the EMA-like hyperparameter of EDM2 models to 0.1.
4. **Weight decay** refers to creating ϵ_{neg} using an increased L2 weight regularization compared to ϵ_{pos} , which in-

Table 1. FDD (\downarrow) and FID (\downarrow), with the guidance weight in subscript. The WMG methods are detailed in Section 4.1. FFHQ-64 is the only unconditional task; all other experiments used class labels as model conditions for both networks. [†] The negative model additionally has reduced capacity (EDM2-XS).

	EDM			EDM2-S	
	CIFAR-10	CIFAR-100	FFHQ-64	ImageNet-512	
	FDD	FDD	FDD	FDD	FID
No Guidance	139.4	196.6	174.8	112.2	2.92
CFG [16]	99.9 _{0.6}	126.6 _{0.6}	–	52.9 _{0.8} [†]	2.44 _{0.1} [†]
Weak model guidance (WMG) methods					
- Reduced training	60.8 _{1.1}	81.2 _{1.3}	94.0 _{1.0}	46.5 _{1.2}	1.79 _{0.8}
- Reduced capacity	62.4 _{0.9}	93.8 _{1.1}	102.5 _{1.3}	70.0 _{1.4}	2.20 _{0.7}
- Reduced capacity and training (RCT)	62.1 _{0.8}	87.0 _{1.0}	95.3 _{1.0}	42.1_{1.4}	1.67_{0.8}
- Weight decay fine-tuning	65.0 _{1.3}	88.1 _{1.4}	111.2 _{2.4}	52.1 _{0.6}	2.46 _{0.1}
- Weight decay re-training	64.7 _{1.3}	93.3 _{1.3}	133.0 _{1.4}	–	–
- Weight decay and reduced training	59.0_{0.9}	75.9_{1.1}	92.6_{1.0}	43.9 _{0.9}	2.25 _{0.2}

creases the model bias in the context of the bias-variance tradeoff [47]. In practice, ϵ_{neg} is the result of either re-training ϵ_{pos} from scratch (*Weight decay re-training*) or fine-tuning ϵ_{pos} (*Weight decay fine-tuning*) under sufficiently strong weight decay regularization.

5. **Weight decay and reduced training** combines (1) and (4) and requires ϵ_{neg} to be obtained through re-training.

4.2. Sliding window guidance (SWG)

To improve the perceptual quality of images, we introduce a new guidance method that upweights long-range dependencies on image level. The idea is to generate ϵ_{neg} by restricting the spatial input size ($H \times W$) of ϵ_{pos} to a smaller size $k \times l$, with $k < H$ and $l < W$, which induces a defined cut-off for long-range dependencies. In practice, this is possible if ϵ_{pos} can process multiple image resolutions. To cover the whole image, we use sliding windows to generate N crops of size $k \times l$, using fixed strides for each spatial dimension. These crops are independently processed by ϵ_{pos} as illustrated in Fig. 3. The N predictions of ϵ_{pos} are superimposed in the same order and at the same positions as the crops were taken, which results in a $H \times W$ output for ϵ_{neg} . Overlapping pixels are averaged. A pseudo-code for SWG is provided in the supplementary material. We emphasize that inference using sliding windows is a common technique in high-resolution 2D/3D image processing and is ingrained into existing tools and frameworks [9, 21, 43]. Like all guidance methods based on Eq. (2), SWG can be linearly combined with other guidance techniques, using $\tilde{\epsilon}(\mathbf{x}, t) = \epsilon_{\text{pos}}(\mathbf{x}, t) + \sum_i w_i [\epsilon_{\text{pos}}(\mathbf{x}, t) - \epsilon_{\text{neg}}^{(i)}(\mathbf{x}, t)]$, where the superscripts indicate different guidance methods. In Ta-

ble 2, we combine SWG with RCT (RCT+SWG) and CFG (CFG+SWG).

Hyperparameters and limitations. One limitation of SWG is that the noise predictor, ϵ_{pos} , must process inputs of varying image resolution. Nonetheless, current architectures, such as Unets [17] or (diffusion) image transformers [37], generally satisfy this requirement. SWG can be implemented in a few lines of code and requires no training modifications or class conditioning. Unless otherwise specified, we assume $H = W$ and use crop size $k = l \approx 5/8 \times H$ and $N = 4$, which translates into $k = 40, s = 24$ at 64×64 resolution. We denote the overlap ratio per dimension as $r = 1 - \frac{s}{k} = 0.4$. We keep the same design choice for latent DMs [38] that operate in $\frac{H}{8} \times \frac{H}{8}$ feature dimensions.

The computational overhead of SWG compared to CFG is determined by the overlap ratio r and the architecture. For EDM-S and $r = 0.4$, we measured an overhead of less than 30% compared to CFG based on a naive implementation of SWG. More details are provided in the supplementary material.

5. Experimental evaluation

5.1. Implementation details

All the experiments were conducted on 4 Nvidia A100 GPUs with 40GB of VRAM. We adopt commonly used datasets such as CIFAR10, CIFAR100 [28], FFHQ [23], and ImageNet [11] at various resolutions. Following recent works [10, 20, 25, 26, 30, 46], we produce 50K samples for the evaluations and measure the Frechet distance [15] using features from InceptionV3 and DINOv2 ViT-L [34],

denoted by FID and FDD, respectively. To demonstrate the applicability of SWG, we apply it to state-of-the-art class conditional models, such as DiT-XL [37], ADM [12] and EDMv2 [26]. We use FDD as our primary metric since it has recently shown better alignment with human judgment [29, 32, 36, 46]. Additional implementation details are provided in the supplementary material.

Human evaluation. The human evaluation conducted in this study aims to determine if there is a measurable preference for SWG at the image level. In the first evaluation round, we compare (i) the unguided outcome ($w = 0$), (ii) the guidance scale that yields the lowest FDD score ($w = 0.2$ for SWG), and (iii) an arbitrarily high guidance scale. Based on visual inspection, we selected $w=1$ for SWG. In the second round, we compare (i) the unguided outcome ($w = 0$), (ii) SWG with $w = 1$ (the best performer from the first round), and (iii) RCT with a high guidance scale. Similarly, we picked $w = 2$ for RCT based on visual inspection. Fifteen participants viewed randomly sampled triplets from a set of 20K images and were asked to select the highest-quality image based on their preference. The images were created using the current state-of-the-art EDMv2-XXL with the same initial noise. In contrast to previous human evaluations on diffusion guidance [19], we added the options *Unrealistic*, meaning that all images are semantically inconsistent, and *Identical*, meaning that images are almost visually *Identical*. Exemplar images are provided in the supplementary material.

5.2. Experimental results

WMG. Table 1 shows consistent FDD improvements for all WMG variants on small-scale benchmarks (CIFAR-10, CIFAR-100, FFHQ-64), outperforming both the unguided generation and CFG (when applicable) by large margins. We highlight that improvements w.r.t FID are inconsistent on small-scale benchmarks for all guidance methods. FID is well known to be agnostic to features unrelated to ImageNet and has saturated on small-scale benchmarks in recent years¹ [13, 29, 32, 36, 40, 46].

Interestingly, weight decay re-training and fine-tuning attain similar results to other WMG variants. We clarify that the considered EDM models do not have weight decay regularization by default. Since increased regularization increases the model’s bias, these results verify our intuition of “similar error but stronger” from the toy example (Sec. 3) in higher dimensions. On top of that, weight decay fine-tuning and weight decay with reduced training require little computational resources to achieve competitive results. For instance, weight decay fine-tuning requires $\approx 90M$ seen images on ImageNet-512, which translates to roughly 4% of the training budget of ϵ_{pos} (2147M seen samples).

¹<https://paperswithcode.com/sota/image-generation-on-cifar-10>

Table 2. FDD (\downarrow) and FID (\downarrow) for several sampling methods on ImageNet for different architectures and resolutions. We highlight methods that require training-related modifications in grey [12, 16]. The subscripts indicate the guidance scales, while the asterisk(*) shows our reproduction of SAG.

Model/Res	Guidance	FID	FDD
EDM2-S /512	\times	2.91	112.2
	SWG _{.1/.5}	2.59	56.1
	RCT _{.8/1.4}	1.67	42.1
	RCT ₁ + SWG _{0.2}	–	39.2
EDM2-XXL /512	\times	2.29	49.7
	SWG _{.05/.2}	2.61	37.7
	RCT _{.2/1}	2.23	30.3
	RCT ₁ + SWG _{.1}	–	30.0
DiT-XL /256	\times	9.83	213.2
	SWG _{.25/.5}	4.00	80.6
	CFG _{.5}	2.40	76.4
	CFG _{.4} + SWG _{.2}	–	52.6
ADM/128	\times	5.98	150.9
	SAG _{.1} [19]	5.11	–
	SAG* _{.1}	6.72	154.6
	SWG _{.1/.3}	5.93	105.6
	CG _{.5/1}	3.01	82.6
<i>Unconditional generation</i>			
EDM2-XS/ 512	\times	19.53	350
	SWG _{.2/.4}	14.23	228

In the small-scale datasets, we tuned the number of parameters and found the range of 12% to 25% to work well for the reduced capacity variant. However, on ImageNet-512, the only publicly available DM of reduced capacity is EDM2-XS, which has roughly 44.5% of the parameters of EDM2-S. This might explain the underperformance of the reduced capacity variant on ImageNet-512. It also highlights the difficulty of finding the appropriate learning capacity for this variant, which requires up to 4MWh on ImageNet-512 to train ϵ_{neg} [26]. Finally, RCT yields the largest relative FDD / FID improvements on ImageNet with 20% / 31.6% compared to CFG[†] using an ϵ_{neg} with the same number of parameters.

SWG. SWG consistently outperforms the unguided generation for all considered models, image resolutions, and generative metrics except for FID on EDM2-XXL as de-



Figure 4. Samples generated by different guidance methods with different guidance weights but the same initial noise. The noise predictor ϵ_{pos} is based on the EDM2-XXL network trained on ImageNet-512, with model condition “orange”. Columns: guidance weights w are scaled by \tilde{w} , with \tilde{w} the individual weight for each method corresponding to lowest FDD. The first column shows samples using ϵ_{neg} as noise predictor, which corresponds to setting $w = -1$ in Eq. (2). Rows: RCT (reduced capacity and reduced training) with $\tilde{w} = 1$, SWG (sliding window guidance) with $\tilde{w} = 0.2$, and CFG[†] (classifier-free guidance) with $\tilde{w} = 0.6$.

pictured in Table 2. We observe that better-performing DMs exhibit smaller relative gains from guidance. For instance, DiT [5, 37] benefits significantly from SWG, yielding a relative improvement of 59% and 62% w.r.t. FID and FDD respectively. For the ADM model operating directly in 128×128 image space, SWG demonstrates a substantial relative gain in FDD of 30% over the unguided generation. Regarding SAG[19], we were unable to reproduce the authors’ results using the official implementation. Overall, results from Table 2 provide strong evidence that a significant part of the sampling error of DMs originates from its inability to capture long-range dependencies, leading to incoherent images of low perceptual quality.

Combining SWG with RCT and CFG. Table 2 shows further improvements when combining SWG with RCT and CFG. There, we report a relative FDD improvement of 65% over the unguided samples for EDM2-S and 6.9% over RCT. We report an even larger relative gain of 26.4% when combining SWG with CFG. Our results suggest that SWG has a complementary impact on both CFG and RCT. We abstain from optimizing FID when combining SWG with other methods due to the high computational cost of hyperparameter search.

5.3. Ablation studies

Guidance interval. Similar to CFG [30], in Table 3a, we demonstrate that applying guidance only at an intermediate interval further improves SWG by a relative 11.8% and 8.7% in FDD on CIFAR-10 and ImageNet-512 respectively. In line with the toy example (Section 3) and concurrent work [25], using a guidance interval does not significantly improve results for WMG methods (see supplementary material).

Impact of kernel size and N . Table 3b shows that several combinations of kernel size and N crops can attain similar results on both FID and FDD. Intriguingly, while FID prefers higher overlap ratios r (for $N = 4$), FDD shows that the overlap between crops is not required to obtain improvements over the unguided model. This suggests that (i) even without overlapping crops, SWG introduces no artifacts w.r.t. generative metrics, and (ii) minimal to no tuning is required as opposed to heuristic model-specific impairments like SAG.

Weight decay fine-tuning. Table 3c shows the sensitivity of the weight decay hyperparameter λ on ImageNet-512, where ϵ_{pos} is trained with $\lambda = 0$. The fine-tuning training time and guidance weight have been optimized for all reported values. We observe that both metrics exhibit a low

Table 3. (a) Ablation study for sliding window guidance (SWG) for various kernel sizes k and N patches using EDM2-S on ImageNet-512 operating at 64x64 latent resolution. (b) SWG, but applying guidance only at a fixed intermediate interval [30] using EDM and EDM2-S on CIFAR10 and ImageNet-512. (c) Weight decay fine-tuning ablation using the same benchmark. [†] The negative model additionally has reduced capacity (EDM2-XS).

	CIFAR-10	IN-512	N, k, r	FDD	FID	λ	FDD	FID
Guidance	FDD	FDD	\mathbf{x}	112.2	2.92	\mathbf{x}	112.2	2.92
\mathbf{x}	139.4	112.2	4, 32, 0	55.7 _{0.3}	2.72 _{0.1}	5e-4	63.6 _{0.6}	2.52 _{0.1}
CFG	99.9 _{0.6}	52.9 _{0.8} [†]	4, 40, 0.4	56.1 _{0.5}	2.59 _{0.1}	1e-4	61.4 _{0.5}	2.47 _{0.1}
+ interval	93.4 _{1.2}	46.5 _{1.8} [†]	4, 48, 0.6	60.7 _{0.5}	2.56 _{0.1}	5e-5	55.2 _{0.5}	2.46 _{0.1}
SWG	87.0 _{0.3}	56.1 _{0.5}	9, 32, 0.5	55.4 _{0.3}	2.69 _{0.1}	2e-5	52.1 _{0.6}	2.46 _{0.1}
+ interval	76.7 _{0.9}	51.2 _{1.2}	9, 24, 0.625	58.1 _{0.2}	2.89 _{0.1}	1e-5	60.3 _{1.2}	2.51 _{0.2}
			16,16,0	64.0 _{0.2}	3.15 _{0.1}			

(a) Applying guidance only at an intermediate interval.

(b) Varying the kernel size k and number of patches N .

(c) Impact of weight decay’s strength (λ) during fine-tuning.

sensitivity to the choice of λ . FDD only loses up to 19.1% of its gain over the unguided generation, even for λ as high as $25\times$ the optimal setting ($5 \cdot 10^{-4}$ vs $2 \cdot 10^{-5}$).

5.4. Qualitative results

To visualize the differences between the guidance methods investigated in this work, we examine ImageNet-512 samples generated from the same initial noise (Fig. 4). All three methods, RCT, SWG, and CFG, tend to exhibit improved perceptual quality for moderate guidance weights but show reduced variation (SWG, CFG) or artifacts (RCT) for higher guidance weights. To understand these effects, it is helpful to examine the unguided samples produced by ϵ_{neg} , which corresponds to setting $w = -1$ in Eq. (2). Comparing the first two columns of Fig. 4, we see that the global image composition (box of fruits) for ϵ_{pos} ($w = 0$) is only recovered by ϵ_{neg} ($w = -1$) for RCT, whereas the global composition has significantly changed for SWG and strongly changed for CFG. As guidance extrapolates in the direction of the differences between the positive and negative model, we observe for $w = \tilde{w}$ that the global composition is essentially conserved for RCT, slightly conserved for SWG, and not conserved for CFG [25, 30]. We hypothesize that RCT maintains the diversity of the generated samples closer to the diversity of the real data, which substantially contributes to its superior metric performance.

5.5. Human evaluation

Results from Table 2 show a discrepancy between metrics for EDM2-XXL: FID saturates, while FDD shows a relative improvement of roughly 24% using SWG. Human raters show a notable preference for samples generated with SWG compared to the unguided generation, as illustrated in Figure 5 (left), especially for the chosen high guidance scale of

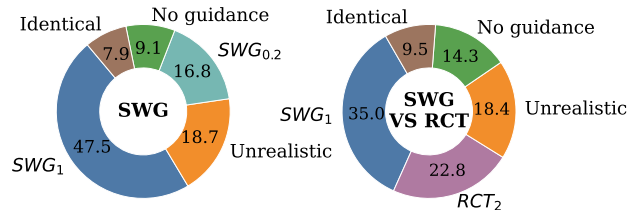


Figure 5. Results from the two rounds of human evaluations. Unrealistic refers to all three images having incoherent semantics (poor quality). Best viewed in color.

1. Surprisingly, the second round (Figure 5, right) revealed that humans show a stronger preference for SWG ($w = 1$) samples compared to RCT ($w = 2$) when both are produced with high guidance scales. Generative metrics could not capture such nuances. We attribute the success of SWG to the fact that humans are strongly biased towards global coherence and consistency of objects, whereas diversity within and among images plays a minor role [8, 13, 31, 49].

Still, the collected data reveals that neither guidance method can improve a significant portion of the images. In particular, at least 26.6% of the images were identical or did not represent a realistic natural image. The latter suggests that while generative metrics seem to saturate, there is still room for generating high-fidelity images. We encourage the reader to visit the supplementary material for more visual comparisons.

6. Conclusion

In this work, we identified “same error but stronger” as a general concept for designing guidance methods. We validated this concept experimentally for a toy example and in higher dimensions by investigating several WMG meth-

ods. However, the question remains how to practically construct negative models if the nature of the prediction error for the positive model is unclear. A possible route for realizing good negative models is to jointly limit network scaling factors [22], such as dataset size, number of parameters, and training time. Our results support this route, as combining different guidance methods consistently achieves the best performance.

7. Acknowledgements

Computing resources were provided by the German AI Service Center WestAI under the project name “westai9566”. In particular, the authors would like to express their gratitude to Prof. Dr. Timo Dickscheid and Fritz Niesel for their guidance regarding the computational resources used for the project. The authors also wish to thank Kaspar Senft, Georgios Zoumpourlis, and Felix Michels for their constructive feedback, which greatly enhanced the quality of this manuscript.

References

- [1] Nikolas Adaloglou, Tim Kaiser, Felix Michels, and Markus Kollmann. Rethinking cluster-conditioned diffusion models. *arXiv preprint arXiv:2403.00570*, 2024. [1](#)
- [2] Donghoon Ahn, Hyoungwon Cho, Jaewon Min, Wooseok Jang, Jungwoo Kim, SeonHwa Kim, Hyun Hee Park, Kyong Hwan Jin, and Seungryong Kim. Self-rectifying diffusion sampling with perturbed-attention guidance. *arXiv preprint arXiv:2403.17377*, 2024. [2](#)
- [3] Md Manjurul Ahsan, Shivakumar Raman, Yingtao Liu, and Zahed Siddique. A comprehensive survey on diffusion models and their applications. 2024. [1](#)
- [4] Sina Alemohammad, Ahmed Imtiaz Humayun, Shruti Agarwal, John Collomosse, and Richard Baraniuk. Self-improving diffusion models with synthetic data. *arXiv preprint arXiv:2408.16333*, 2024. [2](#)
- [5] Jie An, De Wang, Pengsheng Guo, Jiebo Luo, and Alexander Schwing. On inductive biases that enable generalization of diffusion transformers. *arXiv preprint arXiv:2410.21273*, 2024. [7](#)
- [6] Yogesh Balaji, Seungjun Nah, Xun Huang, Arash Vahdat, Jiaming Song, Qinsheng Zhang, Karsten Kreis, Miika Aittala, Timo Aila, Samuli Laine, et al. ediff-i: Text-to-image diffusion models with an ensemble of expert denoisers. *arXiv preprint arXiv:2211.01324*, 2022. [2](#)
- [7] Arwen Bradley and Preetum Nakkiran. Classifier-free guidance is a predictor-corrector. *arXiv preprint arXiv:2408.09000*, 2024. [1](#)
- [8] Charles F Cadieu, Ha Hong, Daniel LK Yamins, Nicolas Pinto, Diego Ardila, Ethan A Solomon, Najib J Majaj, and James J DiCarlo. Deep neural networks rival the representation of primate it cortex for core visual object recognition. *PLoS computational biology*, 10(12):e1003963, 2014. [8](#)
- [9] M Jorge Cardoso, Wenqi Li, Richard Brown, Nic Ma, Eric Kerfoot, Yiheng Wang, Benjamin Murrey, Andriy Myronenko, Can Zhao, Dong Yang, et al. Monai: An open-source framework for deep learning in healthcare. *arXiv preprint arXiv:2211.02701*, 2022. [5](#)
- [10] Min Jin Chong and David Forsyth. Effectively unbiased fid and inception score and where to find them, 2020. [5](#)
- [11] Jia Deng, Wei Dong, Richard Socher, Li-Jia Li, Kai Li, and Li Fei-Fei. Imagenet: A large-scale hierarchical image database. In *2009 IEEE conference on computer vision and pattern recognition*, pages 248–255. Ieee, 2009. [5](#)
- [12] Prafulla Dhariwal and Alexander Nichol. Diffusion models beat gans on image synthesis. *Advances in neural information processing systems*, 34:8780–8794, 2021. [1, 6](#)
- [13] Robert Geirhos, Patricia Rubisch, Claudio Michaelis, Matthias Bethge, Felix A Wichmann, and Wieland Brendel. Imagenet-trained cnns are biased towards texture; increasing shape bias improves accuracy and robustness. *arXiv preprint arXiv:1811.12231*, 2018. [6, 8](#)
- [14] Amir Hertz, Ron Mokady, Jay Tenenbaum, Kfir Aberman, Yael Pritch, and Daniel Cohen-Or. Prompt-to-prompt image editing with cross attention control. *arXiv preprint arXiv:2208.01626*, 2022. [2](#)
- [15] Martin Heusel, Hubert Ramsauer, Thomas Unterthiner, Bernhard Nessler, and Sepp Hochreiter. Gans trained by a two time-scale update rule converge to a local nash equilibrium, 2018. [5](#)
- [16] Jonathan Ho and Tim Salimans. Classifier-free diffusion guidance, 2022. [1, 2, 4, 5, 6](#)
- [17] Jonathan Ho, Ajay Jain, and Pieter Abbeel. Denoising diffusion probabilistic models, 2020. [1, 5](#)
- [18] Susung Hong. Smoothed energy guidance: Guiding diffusion models with reduced energy curvature of attention. *arXiv preprint arXiv:2408.00760*, 2024. [2](#)
- [19] Susung Hong, Gyuseong Lee, Wooseok Jang, and Seungryong Kim. Improving sample quality of diffusion models using self-attention guidance. In *Proceedings of the IEEE/CVF International Conference on Computer Vision*, pages 7462–7471, 2023. [2, 4, 6, 7, 11, 12, 14](#)
- [20] Sadeep Jayasumana, Srikumar Ramalingam, Andreas Veit, Daniel Glasner, Ayan Chakrabarti, and Sanjiv Kumar. Rethinking fid: Towards a better evaluation metric for image generation. In *Proceedings of the IEEE/CVF Conference on Computer Vision and Pattern Recognition*, pages 9307–9315, 2024. [5](#)
- [21] AQ Jiang, A Sablayrolles, A Mensch, C Bamford, DS Chaplot, D de las Casas, F Bressand, G Lengyel, G Lample, L Saulnier, et al. Mistral 7b (2023). *arXiv preprint arXiv:2310.06825*, 2023. [5](#)
- [22] Jared Kaplan, Sam McCandlish, Tom Henighan, Tom B Brown, Benjamin Chess, Rewon Child, Scott Gray, Alec Radford, Jeffrey Wu, and Dario Amodei. Scaling laws for neural language models. *arXiv preprint arXiv:2001.08361*, 2020. [2, 4, 9, 11](#)
- [23] Tero Karras, Samuli Laine, and Timo Aila. A style-based generator architecture for generative adversarial networks. In *Proceedings of the IEEE/CVF conference on computer vision and pattern recognition*, pages 4401–4410, 2019. [5](#)

- [24] Tero Karras, Miika Aittala, Timo Aila, and Samuli Laine. Elucidating the design space of diffusion-based generative models, 2022. [1](#), [3](#), [24](#), [25](#), [27](#)
- [25] Tero Karras, Miika Aittala, Tuomas Kynkäänniemi, Jaakko Lehtinen, Timo Aila, and Samuli Laine. Guiding a diffusion model with a bad version of itself, 2024. [1](#), [2](#), [4](#), [5](#), [7](#), [8](#), [12](#)
- [26] Tero Karras, Miika Aittala, Jaakko Lehtinen, Janne Hellsten, Timo Aila, and Samuli Laine. Analyzing and improving the training dynamics of diffusion models, 2024. [4](#), [5](#), [6](#), [11](#)
- [27] Diederik P. Kingma, Tim Salimans, Ben Poole, and Jonathan Ho. Variational diffusion models, 2023. [1](#)
- [28] Alex Krizhevsky, Geoffrey Hinton, et al. Learning multiple layers of features from tiny images. 2009. [5](#)
- [29] Tuomas Kynkäänniemi, Tero Karras, Miika Aittala, Timo Aila, and Jaakko Lehtinen. The role of imagenet classes in fréchet inception distance, 2023. [6](#)
- [30] Tuomas Kynkäänniemi, Miika Aittala, Tero Karras, Samuli Laine, Timo Aila, and Jaakko Lehtinen. Applying guidance in a limited interval improves sample and distribution quality in diffusion models, 2024. [2](#), [5](#), [7](#), [8](#), [14](#)
- [31] Barbara Landau, Linda B Smith, and Susan S Jones. The importance of shape in early lexical learning. *Cognitive development*, 3(3):299–321, 1988. [8](#)
- [32] Stanislav Morozov, Andrey Voynov, and Artem Babenko. On self-supervised image representations for gan evaluation. In *International Conference on Learning Representations*, 2021. [6](#)
- [33] Jisu Nam, Heesu Kim, DongJae Lee, Siyoon Jin, Seungryong Kim, and Seunggyu Chang. Dreammatcher: Appearance matching self-attention for semantically-consistent text-to-image personalization. In *Proceedings of the IEEE/CVF Conference on Computer Vision and Pattern Recognition*, pages 8100–8110, 2024. [2](#)
- [34] Maxime Oquab, Timothée Darcet, Theo Moutakanni, Huy V. Vo, Marc Szafraniec, Vasil Khalidov, Pierre Fernandez, Daniel Haziza, Francisco Massa, Alaaeldin El-Nouby, Russell Howes, Po-Yao Huang, Hu Xu, Vasu Sharma, Shang-Wen Li, Wojciech Galuba, Mike Rabbat, Mido Assran, Nicolas Ballas, Gabriel Synnaeve, Ishan Misra, Herve Jegou, Julien Mairal, Patrick Labatut, Armand Joulin, and Piotr Bojanowski. Dinov2: Learning robust visual features without supervision, 2023. [5](#)
- [35] D. B. Owen. A table of normal integrals. *Communications in Statistics - Simulation and Computation*, 9(4):389–419, 1980. [25](#), [26](#)
- [36] Gaurav Parmar, Richard Zhang, and Jun-Yan Zhu. On aliased resizing and surprising subtleties in gan evaluation, 2022. [6](#)
- [37] William Peebles and Saining Xie. Scalable diffusion models with transformers. In *Proceedings of the IEEE/CVF International Conference on Computer Vision*, pages 4195–4205, 2023. [1](#), [5](#), [6](#), [7](#), [12](#)
- [38] Robin Rombach, Andreas Blattmann, Dominik Lorenz, Patrick Esser, and Björn Ommer. High-resolution image synthesis with latent diffusion models. In *Proceedings of the IEEE/CVF conference on computer vision and pattern recognition*, pages 10684–10695, 2022. [5](#)
- [39] Seyedmorteza Sadat, Jakob Buhmann, Derek Bradley, Otmar Hilliges, and Romann M. Weber. Cads: Unleashing the diversity of diffusion models through condition-annealed sampling. In *ICLR*, 2024. [2](#)
- [40] Seyedmorteza Sadat, Manuel Kansy, Otmar Hilliges, and Romann M Weber. No training, no problem: Rethinking classifier-free guidance for diffusion models. *arXiv preprint arXiv:2407.02687*, 2024. [2](#), [6](#)
- [41] Chitwan Saharia, William Chan, Saurabh Saxena, Lala Li, Jay Whang, Emily L Denton, Kamyar Ghasemipour, Raphael Gontijo Lopes, Burcu Karagol Ayan, Tim Salimans, et al. Photorealistic text-to-image diffusion models with deep language understanding. *Advances in neural information processing systems*, 35:36479–36494, 2022. [1](#), [2](#)
- [42] Tim Salimans and Jonathan Ho. Progressive distillation for fast sampling of diffusion models, 2022. [1](#)
- [43] Jiahao Shao, Yuanbo Yang, Hongyu Zhou, Youmin Zhang, Yujun Shen, Matteo Poggi, and Yiyi Liao. Learning temporally consistent video depth from video diffusion priors. *arXiv preprint arXiv:2406.01493*, 2024. [5](#)
- [44] Jascha Sohl-Dickstein, Eric A. Weiss, Niru Maheswaranathan, and Surya Ganguli. Deep unsupervised learning using nonequilibrium thermodynamics, 2015. [1](#)
- [45] Yang Song, Jascha Sohl-Dickstein, Diederik P. Kingma, Abhishek Kumar, Stefano Ermon, and Ben Poole. Score-based generative modeling through stochastic differential equations, 2021. [1](#)
- [46] George Stein, Jesse C. Cresswell, Rasa Hosseinzadeh, Yi Sui, Brendan Leigh Ross, Valentin Vilecroze, Zhaoyan Liu, Anthony L. Caterini, J. Eric T. Taylor, and Gabriel Loaiza-Ganem. Exposing flaws of generative model evaluation metrics and their unfair treatment of diffusion models, 2023. [5](#), [6](#)
- [47] Ulrike Von Luxburg and Bernhard Schölkopf. Statistical learning theory: Models, concepts, and results. In *Handbook of the History of Logic*, pages 651–706. Elsevier, 2011. [5](#)
- [48] Xi Wang, Nicolas Dufour, Nefeli Andreou, Marie-Paule Cani, Victoria Fernández Abrevaya, David Picard, and Vicky Kalogeiton. Analysis of classifier-free guidance weight schedulers. *arXiv preprint arXiv:2404.13040*, 2024. [2](#), [12](#)
- [49] Daniel LK Yamins, Ha Hong, Charles F Cadieu, Ethan A Solomon, Darren Seibert, and James J DiCarlo. Performance-optimized hierarchical models predict neural responses in higher visual cortex. *Proceedings of the national academy of sciences*, 111(23):8619–8624, 2014. [8](#)

A. Human evaluation.

We emphasize that the conducted human evaluation assesses the quality but not the diversity of generated images. Consequently, human evaluation results should not be directly compared with performance measures, such as FID and FDD, which react sensitively to changes in sample diversity. Upon visual inspection, we observed that the guidance scales w that correspond to the best Fréchet distances (w^*), such as FID (InceptionV3 encoder) and FDD (DINOv2 ViT-L encoder), are often far from what we consider a high-quality image. We also find that guidance methods using different negative models (ϵ_{pos}), such as RCT and SWG, cannot be fairly compared at the same guidance scales as well as linear multiples of w^* (Figure 12). One possible reason is that w^* is set by a metric, while w affects the sampling process non-linearly. For this reason, we have decided to pick guidance scales for RCT and SWG based on human assessment.

Rounds and guidance scales. We conducted two evaluation rounds using human raters. In the first evaluation round, we compare (i) the unguided outcome ($w = 0$), (ii) the guidance scale that yields the lowest FDD score ($w = 0.2$ for SWG), and (iii) an arbitrarily high guidance scale. Based on visual inspection for the highest image quality, we selected $w = 1$ for SWG. In the second round, we compare (i) the unguided outcome ($w = 0$), (ii) SWG with $w = 1$ (the best performer from the first round), and (iii) RCT with a high guidance scale. Similarly, we picked $w = 2$ for RCT based on visual inspection for the highest image quality. Fifteen participants viewed randomly sampled triplets from a set of 20K images and were asked to select the highest-quality image based on their preference. Each participant sees a different subset of images from the 20K samples. Importantly, the participants were only instructed to pick the methods that best aligned with their preferences. We did not provide specific instruction that might have benefited SWG, such as focusing on the global coherence of the image. The images were created using the current state-of-the-art EDMv2-XXL [26] with the same initial noise. We provide example images from the human evaluation in Figures 11 and 12 as well as Figures 15 and 16.

Previous studies and added options. Hong et al. [19] conducted a human evaluation, where the authors compared their method, SAG, in the unconditional setup using text-to-image latent diffusion models. We find this design choice unfair as the latent diffusion model uses only a small part of its training budget ($< 20\%$) on the *unconditional* generation. We, therefore, conduct the human evaluation on *conditional* image generation on ImageNet-51.

Additionally, we observed that the generated images usually have negligible differences, or all samples fail to generate a realistic image. This is not reflected in previous human evaluations. In contrast to previous human evaluations [19], we added the options *Unrealistic*, meaning that all images are semantically inconsistent, and *Identical*, meaning that images are almost visually *Identical*. Which image is considered realistic and which image triple is considered identical is subjective and depends on the user. Exemplar images are provided in Figures 13 and 14 to illustrate the above points. The Python application designed for conducting the human evaluation will be open-sourced.

```

1 import torch
2
3 def SWG(x, e_pos, t, labels, N, k, w):
4     # x: noisy images of size [bs, c, H, H]
5     # e_pos: network i.e. Unet
6     # t: timestep
7     # labels: class conditions
8     # N: number of crops in [4,9,16,...]
9     # k: crop size
10    # w: guidance scale
11
12    steps_per_dim = int(torch.sqrt(N))
13    y_pos = e_pos(x, t, labels)
14    bs, c, H, _ = x.shape
15    y_neg = torch.zeros_like(x)
16    overlap = torch.zeros_like(x)
17    stride = (H - k) // (steps_per_dim - 1)
18    for i in range(steps_per_dim):
19        for j in range(steps_per_dim):
20            # left edge (le), right edge (re)
21            le, re = stride * i, stride * i + k
22            # top edge (te), bottom edge (be)
23            te, be = stride * j, stride * j + k
24            # x_p is of shape [bc, c, k, k]
25            x_p = x[:, :, te:be, le:re]
26            y_crop = e_pos(x_p, t, labels)
27            y_neg[:, :, te:be, le:re] += y_crop
28            o_p = torch.ones_like(y_crop)
29            overlap[:, :, te:be, le:re] += o_p
30    # pixel averaging
31    y_neg = y_neg / overlap
32    # Equation 2 in the main text
33    return y_pos + w * (y_pos - y_neg)
34

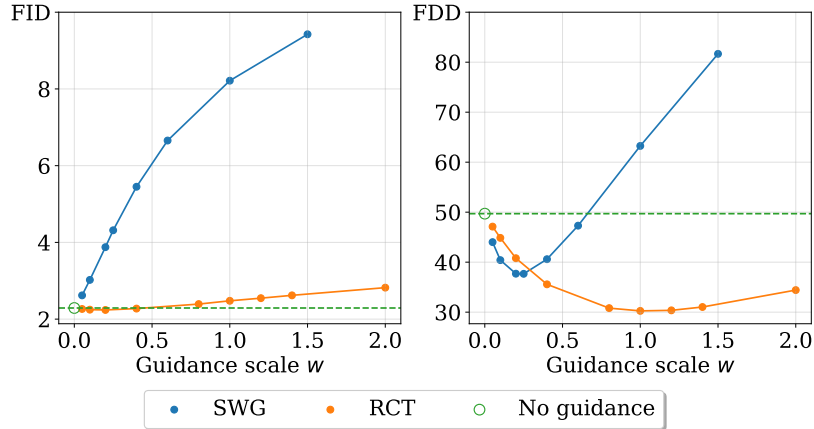
```

Figure 7. Example pseudocode for sliding window guidance (SWG) in Python using the torch library.

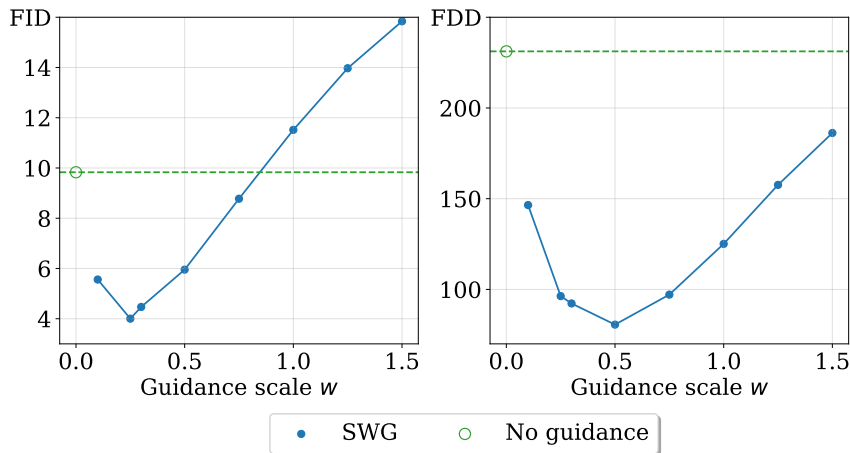
B. Additional implementation details and experiments

Plotting guidance scales w.r.t. Fréchet distances. Similar to [22], we have assumed that the generative error of ϵ_{pos} can be primarily attributed to scaling factors, such as training time and number of parameters. In Figure 6, we illustrate that the largest best-performing publicly available Unet architecture EDM2-XXL shows no improvement w.r.t. FID for SWG and only minimal improvement for reduced capacity and training (RCT). However, this is not in line with DiT-XL/2, where the unguided generation can be significantly improved using SWG w.r.t. to FID and FDD. We suspect that the observed discrepancy can be attributed to the significantly better inductive bias of EDM2-XXL, which leaves less room for improvement using guidance.

SWG implementation details and pseudocode. To make SWG compatible with DiT, we add positional encoding interpolation on DiT-XL to process various resolutions. The choice of $k \approx \frac{5}{8}H$ is determined by practical considerations of Unets. Specifically, k must satisfy $\frac{k}{2^n} \in \mathbb{N}$, where n is the number of downsampling steps of the Unet, and the diffusion model ϵ_{pos} must be able to process multiple image resolutions. We leave text-to-image diffusion models to future work. We provide an implemen-



(a) EDM2-XXL on ImageNet 512x512



(b) DiT-XL/2 on ImageNet 256x256

Figure 6. Frechet distances (y -axis) versus guidance scales (x -axis) using InceptionNetv3 (**FID, left**) and DINOv2 ViT-L (**FDD, right**). Large-scale architectures, such as EDM2-XXL [48] (**top**) and DiT-XL/2 [37] (**bottom**) exhibit different behaviors.

tation of SWG in the Figure 7.

Time overhead at sampling time. In Table 4, we present the time needed to produce 512 samples for various models and guidance methods and their corresponding estimate in images per second per GPU. We emphasize that we have naively implemented SWG, as shown in the pseudocode, and further optimization can help bridge the time overhead. We also found that SAG [19] uses a guidance interval under the hood, making it harder to compare it with SWG fairly.

Applying an intermediate guidance interval to WMG methods. Table 5 demonstrates that WMG methods do not significantly improve from applying a guidance interval, unlike CFG and SWG. The only significant gains are found for EDM on FFHQ-64, showing that this technique is sensitive to the choice of dataset.

State-of-the-art results using SWG. While our results w.r.t. generative metrics using SWG and RCT+SWG do not outperform concurrent the reported FID and FDD values from “autoguidance”

[25] using EDM2, we believe it is a matter of model-specific multi-hyperparameter search and compute time. This study emphasizes the broader applicability and usefulness of SWG, with or without CFG or RCT, rather than tuning for a specific benchmark (model, dataset, metric). Finally, the combination of CFG and SWG demonstrated another promising avenue left for future work, as illustrated in Figure 8.

Guidance interpolation. Figures 9 and 10 provide interpolations of guidance methods following

$$\tilde{\epsilon}(\mathbf{x}, t) = \epsilon_{\text{pos}}(\mathbf{x}, t) + \sum_i \alpha_i w_i [\epsilon_{\text{pos}}(\mathbf{x}, t) - \epsilon_{\text{neg}}^{(i)}(\mathbf{x}, t)] \quad (3)$$

where w_i are the optimized guidance scales w.r.t. FDD for each method and α_i are set to form a convex combination between guidance terms.

ADM at higher resolutions. Experiments at 256×256 image resolution using ADM require over 4 days in our hardware

(384 GPU hours) per guidance scale and are left to future work, as recent state-of-the-art latent diffusion models exhibit far superior image quality. For this reason, we only used the pretrained ADM models at 128x128 resolutions to exemplify that SWG can be applied to any diffusion model.

Table 4. All benchmarks were conducted using 2 Nvidia A100 GPUs with 40GB of VRAM. The authors of SAG apply a guidance interval, which makes the time comparison hard to assess. We benchmark sliding window guidance (SWG), classifier guidance (CG), classifier-free guidance (CFG), classifier-free guidance using a smaller capacity unconditional model (CFG[†]), self-attention guidance (SAG [19]), reduced training (RT) and reduced capacity training (RCT). The symbol \times stands for *No guidance* ($w = 0$). Crucially, SWG is implemented in a naive way with $N = 4$ (as shown in the provided pseudocode) and can be further optimized, which is left to future work. The scalar r denotes the overlap ratio per dimension, where $r = 0$ refers to no overlap.

Model/Res	Guidance	VRAM (GB) per GPU	Batch size	Time for 512 samples in minutes (\downarrow)	Estimate of Imgs/s per GPU (\uparrow)
EDM2-S 512×512	\times	15.2	256	1.36	12.54
	SWG ($r=0.4$)	15.2	256	2.10	8.12
	SWG ($r=0$)	15.2	256	1.85	9.22
	RT	15.2	256	1.77	9.64
	RCT	15.2	256	1.61	10.67
	CFG [†]	15.2	256	1.61	10.67
DiT-XL 256×256	\times	17.9	32	4.61	3.70
	CFG	17.9	32	8.45	2.02
	SWG	17.9	32	11.37	1.50
ADM 128×128	\times	24.3	128	8.65	1.97
	CG	24.3	128	12.17	1.4
	SWG	24.3	128	21.17	0.81
	SAG	24.3	128	16.80	1.01

Table 5. Applying a guidance interval [30] to WMG methods from Table 1 (main text). All interval results were optimized w.r.t the interval setting and guidance weight, and use identical settings otherwise. For the weight decay variant, EDM uses fine-tuning and EDM2-S uses re-training.

	EDM			EDM2-S
	CIFAR-10	CIFAR-100	FFHQ-64	ImageNet-512
	FDD	FDD	FDD	FDD
Reduced training + interval	60.8 _{1.1} 59.7_{1.2}	81.2_{1.3} 81.6 _{1.2}	94.0 _{1.0} 86.9_{1.6}	46.5 _{1.2} 43.8_{1.8}
Reduced capacity + interval	62.4 _{0.9} 61.4_{1.0}	93.8 _{1.1} 91.8_{1.2}	102.5 _{1.3} 92.7_{2.0}	70.0 _{1.4} 64.9_{1.8}
Weight decay + interval	64.7 _{1.3} 63.8_{1.4}	93.3_{1.3} 93.7 _{1.4}	133.0_{1.4} 155.3 _{1.6}	52.1 _{0.6} 51.3_{1.2}

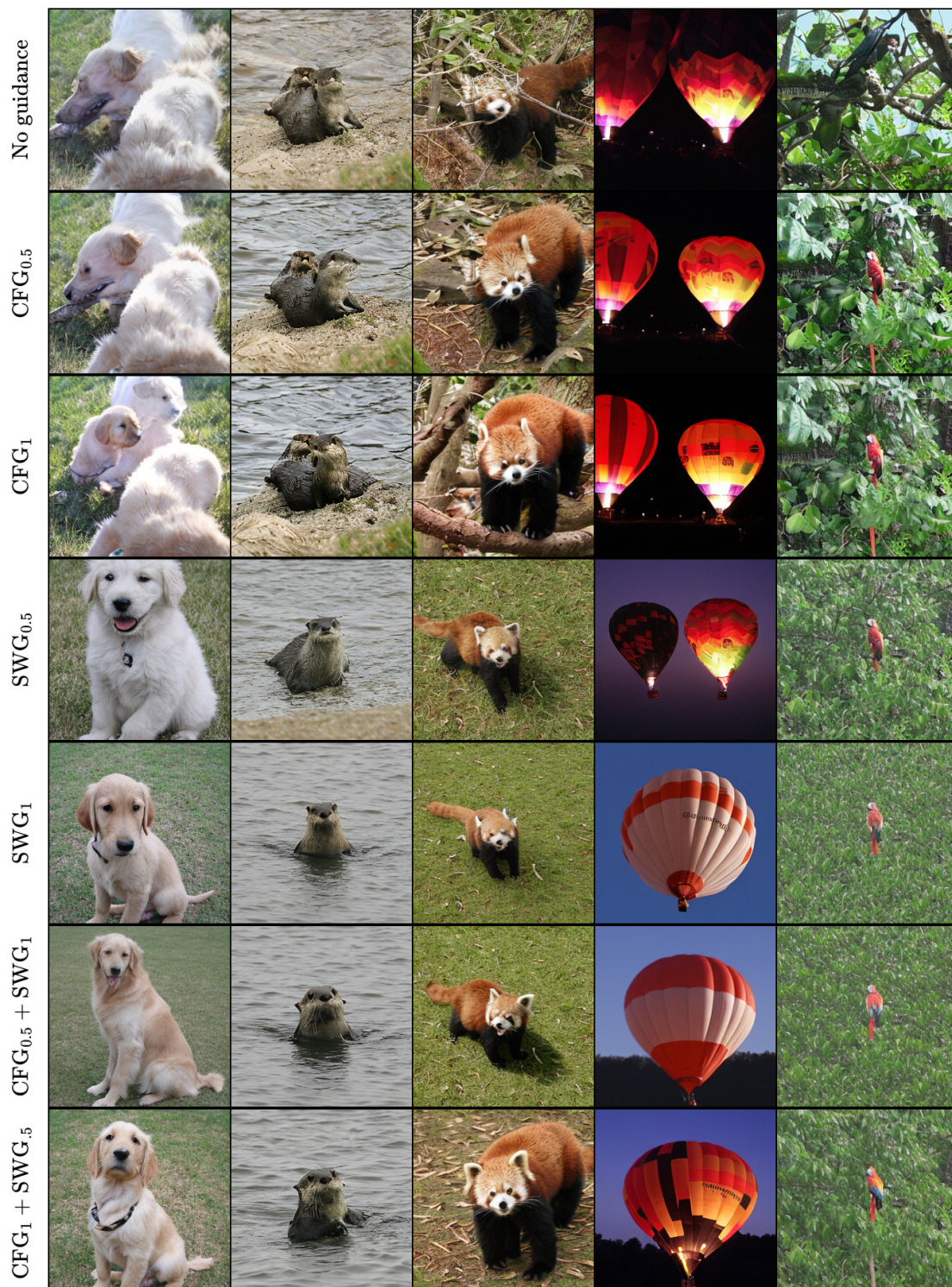


Figure 8. Generated DiT-XL 256×256 samples using CFG, SWG and their combination (CFG+SWG).

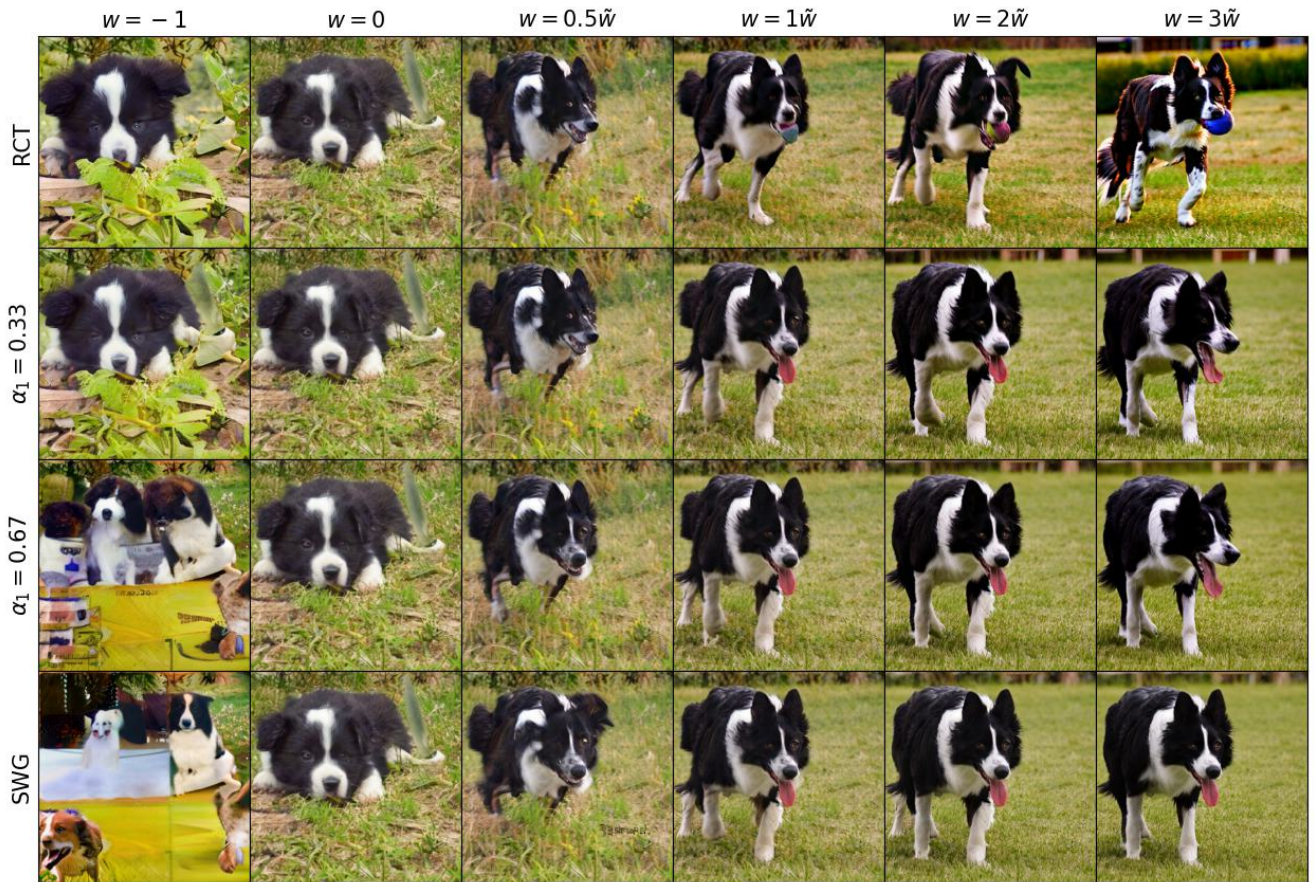


Figure 9. Samples generated by interpolating RCT and SWG with different guidance weights but the same initial noise. The noise predictor ϵ_{pos} is based on the EDM2-XXL network trained on ImageNet-512. Columns: guidance weights w are scaled by \tilde{w} , with \tilde{w} the individual weight for each method corresponding to lowest FDD ($\tilde{w} = 1$ for RCT and $\tilde{w} = 0.2$ for SWG). The first column shows samples using ϵ_{neg} as a noise predictor ($w = -1$). Interpolations are computed according to Equation (3) with a convex combination of the guidance terms parametrized by α_1 and $\alpha_2 = 1 - \alpha_1$.

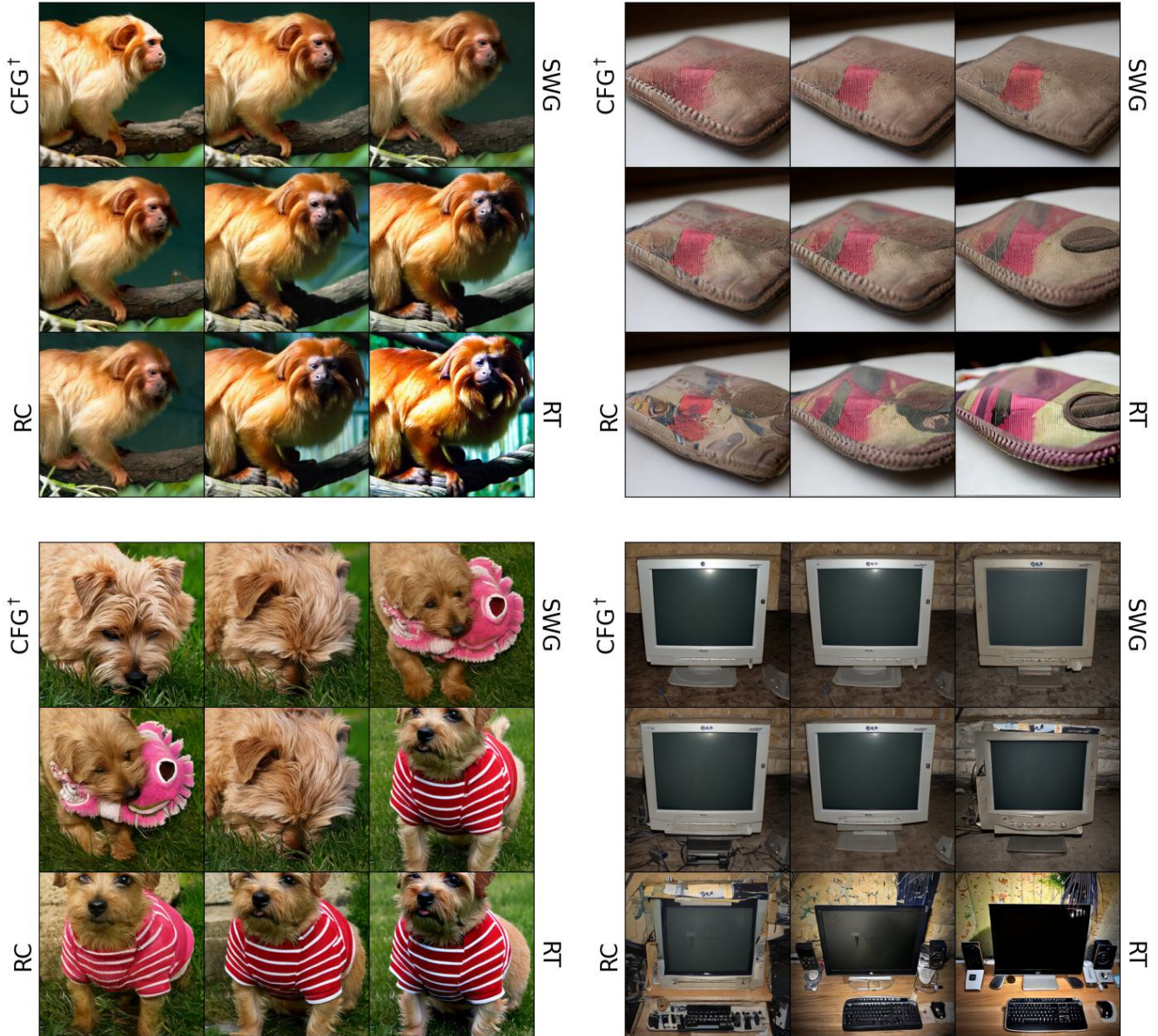


Figure 10. Samples generated by interpolating CFG, SWG, RC (reduced capacity), and RT (reduced training) with different guidance weights but the same initial noise. The noise predictor ϵ_{pos} is based on the EDM2-XXL network trained on ImageNet-512. Respective weights are CFG: $w = 0.6$, SWG: $w = 0.2$, RT: $w = 1.0$ and RC: $w = 1.0$. Interpolations are computed according to Equation (3), such that the sum over guidance terms is a convex combination, with $\alpha_i = 1$ in the corners and linear interpolation in between.

No guidance

RCT₂

SWG₁



Figure 11. Generated samples from the human evaluation where RCT introduced artifacts.



Figure 12. More examples with different guidance scales w for RCT (left) and SWG (right).

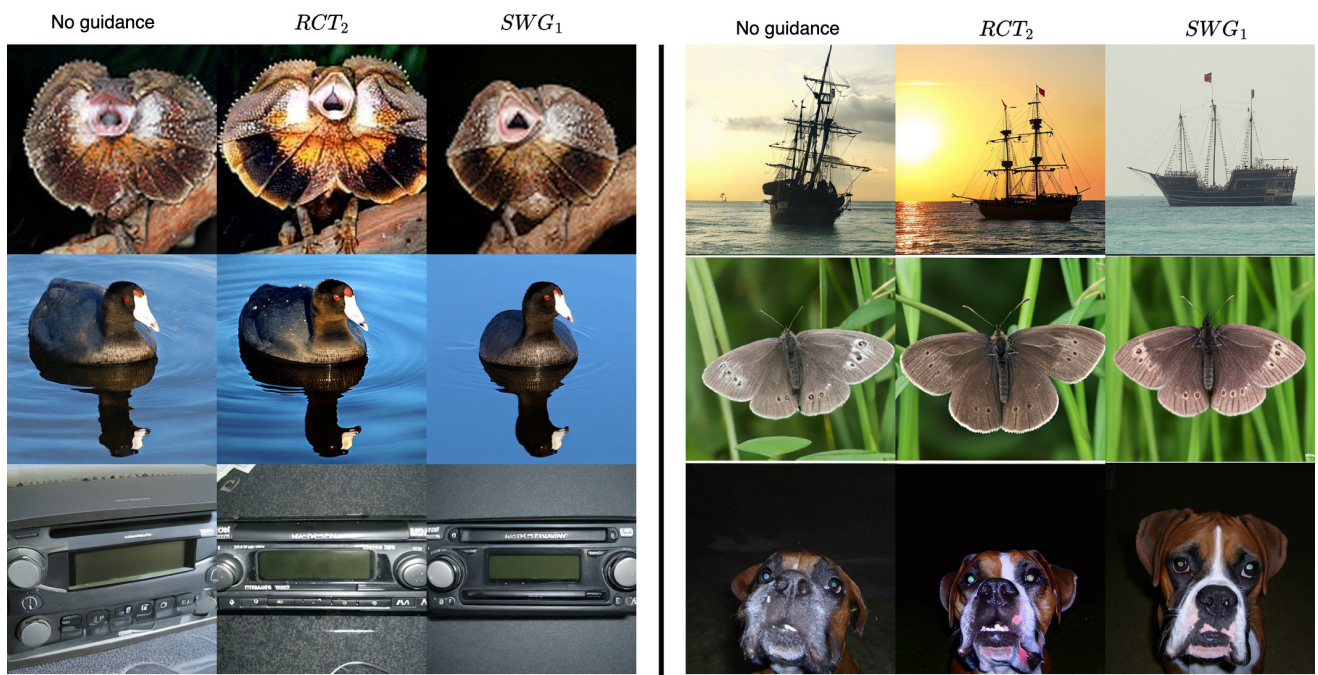


Figure 13. Generated EDM2-XXL 512×512 samples using no guidance (left), RCT (center), and SWG (right) that participants found identical or unrealistic.



Figure 14. Generated EDM2-XXL samples using no guidance (left), RCT (center), and SWG (right) that participants found unrealistic.

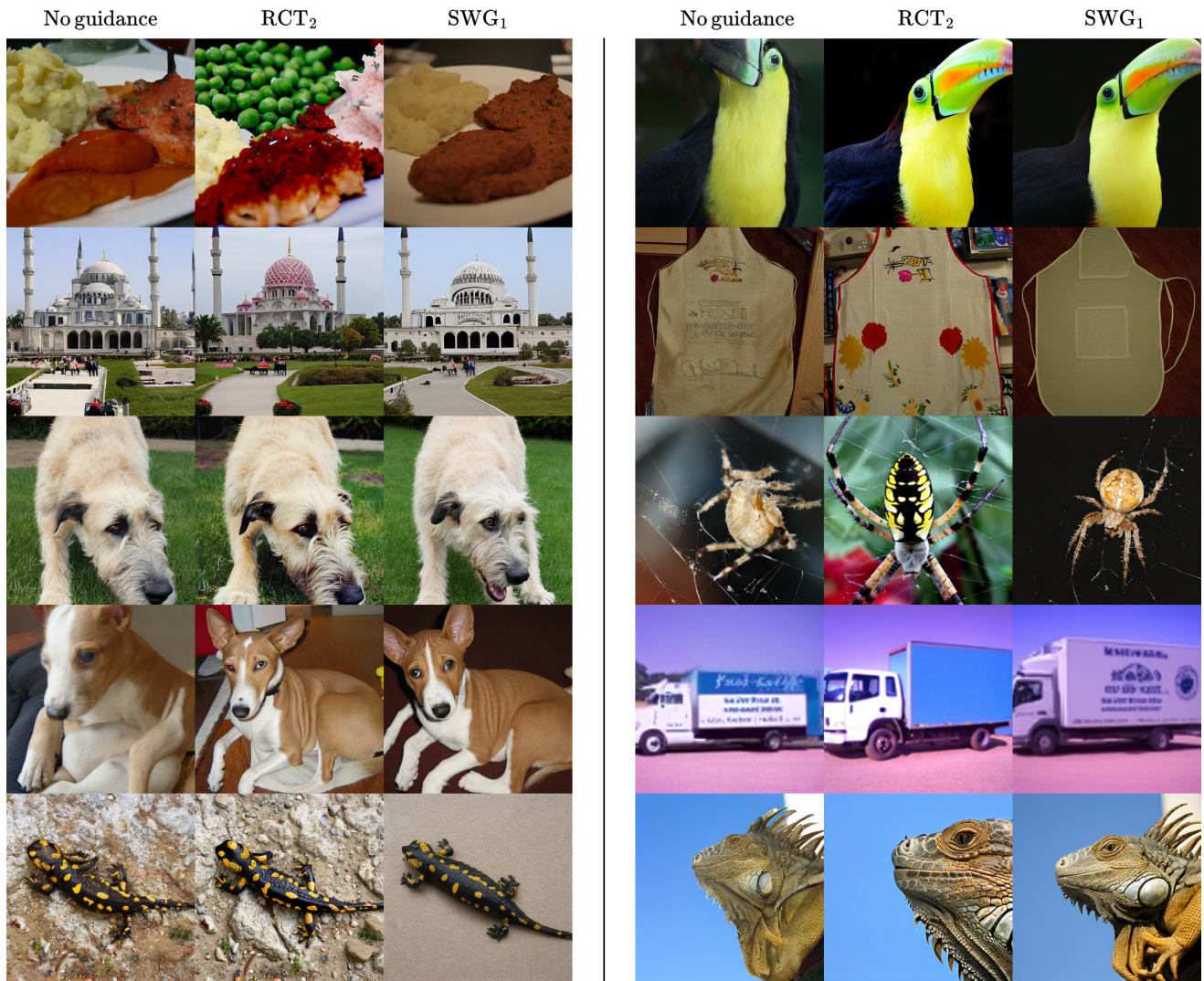


Figure 15. Generated EDM2-XXL samples using no guidance (left), RCT (center), and SWG (right) that participants preferred RCT samples. The subscript indicates the guidance scales used to generate these samples.

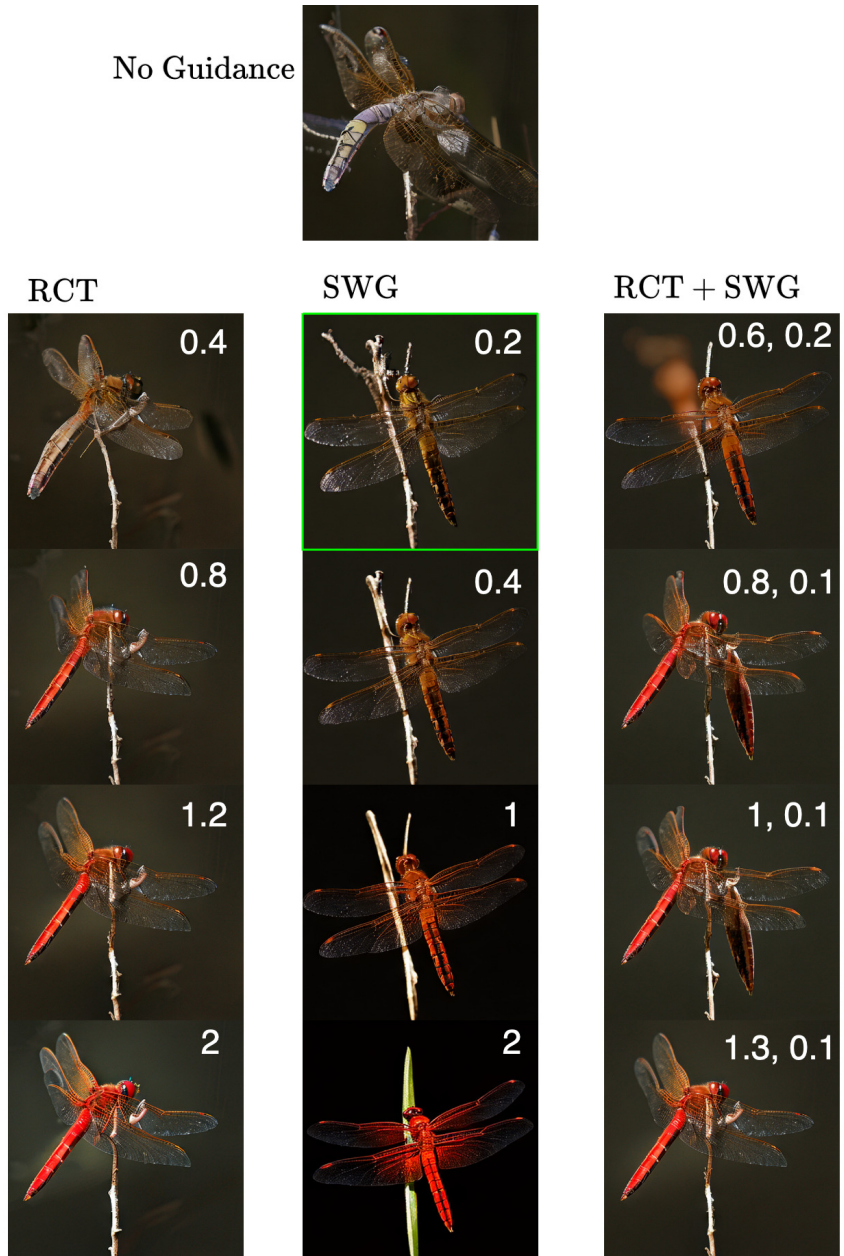


Figure 16. Generated EDM2-XXL 512×512 samples using no guidance, RCT (left), SWG (center), and RCT+SWG (right). The guidance scales are shown in white on the top right corner of the image. The green box shows the sample that was used in the main paper, Figure 1.

Table 6. Settings for Table 1 (main text) on small scale benchmarks using EDM. On CIFAR-10, CIFAR-100, and FFHQ-64. CFG uses an unconditional but otherwise identical to the positive model as negative. Columns specify the checkpoint of the positive model c_{pos} in million images seen, the checkpoint of the negative model c_{neg} in million images seen, the model size (F for full and S for small), and the weight decay parameter λ . The full model corresponds to default architecture hyperparameter settings as detailed in [24]. The small model has a reduced number of resolution levels and channel size ($\text{cres}=1,1$ for CIFAR-10 / CIFAR-100 and $\text{cres}=1,1,1$ for FFHQ) and a reduced number of blocks per level ($\text{num_blocks}=2$ for CIFAR-10 / CIFAR-100). *WD* stands for weight decay, and *RCT* stands for reduced capacity and training.

Settings	EDM											
	CIFAR-10				CIFAR-100				FFHQ-64			
	FDD				FDD				FDD			
	c_{pos}	c_{neg}	Size	λ	c_{pos}	c_{neg}	Size	λ	c_{pos}	c_{neg}	Size	λ
No guidance	500	500	F	0	500	500	F	0	500	500	F	0
CFG	500	500	F	0	500	500	F	0	500	500	F	0
WMG methods												
- Reduced training	500	20	F	0	500	20	F	0	500	20	F	0
- Reduced capacity	500	500	S	0	500	500	S	0	500	500	S	0
- RCT	500	200	S	0	500	100	S	0	500	100	S	0
- WD fine-tuning	500	560	F	5e-4	500	520	F	5e-4	500	540	F	2e-3
- WD re-training	500	500	F	5e-4	500	500	F	5e-4	500	500	F	2e-3
- WD and reduced training	500	30	F	5e-4	500	20	F	5e-4	500	20	F	2e-3

Table 7. Settings for Table 1 (main text) on ImageNet-512 using EDM2-S. Columns specify the checkpoint of the positive model c_{pos} in million images seen, the checkpoint of the negative model c_{neg} in million images seen, the model size (EDM2 variants), and the weight decay parameter λ .

Settings	ImageNet-512, EDM2-S							
	FDD				FID			
	c_{pos}	c_{neg}	Size	λ	c_{pos}	c_{neg}	Size	λ
No guidance	2147	2147	S	0	2147	2147	S	0
CFG [†]	2147	2147	S	0	2147	2147	S	0
WMG methods								
- Reduced training	2147	67	S	0	2147	134	S	0
- Reduced capacity	2147	2147	XS	0	2147	2147	XS	0
- Reduced capacity and training	2147	134	XS	0	2147	268	XS	0
- Weight decay fine-tuning	2147	2233	S	2e-5	2147	2243	S	2e-5
- Weight decay re-training	-	-	-	-	-	-	-	-
- Weight decay and reduced training	2147	63	S	2e-5	2147	63	S	2e-5

C. Toy example details

This section presents the derivation of the noise predictors used for the toy example in the main text. The code for computing the trajectories will be released and allows to visualize guidance effects for different combinations of ϵ_{pos} , ϵ_{neg} , and datasets. We introduce with time $t \in [0, 1]$ a variable that denotes the progress of denoising, which starts from a normally distributed sample, $\mathbf{x}(1)$, and ends at a fully denoised sample, $\mathbf{x}(0)$. In the following, we denote by \mathbf{y} a sample from the data distribution $P(\mathbf{y})$, by $\sigma := \sigma(t)$ the time-dependent noise level, and by $\mathbf{x} := \mathbf{x}(t)$ a point along a denoising trajectory. We set $\sigma(0) = 0$ and choose with $\sigma(1) = 80$ a value such that $\sigma(t) \gg \text{std}(y_i)$, for all dimensions $i \in \{1, 2, \dots, d\}$. We assume $\sigma(t)$ to be a strictly monotone increasing function in time t . To derive the optimal denoiser, we make use of the ordinary differential equation (ODE) that describes the field lines of probability flow (e.g. Eq. (1) of Ref. [24]). This ODE allows the generation of sampling trajectories

$$d\mathbf{x} = -\dot{\sigma}\nabla_{\mathbf{x}} \log P(\mathbf{x}|\sigma^2)dt, \quad (4)$$

when initialized with a noise sample $\mathbf{x}(1) \sim \mathcal{N}(\mathbf{x}|0, \sigma(1)^2)$. Here and in following we use definition $\mathcal{N}(\mathbf{x}|\boldsymbol{\mu}, \sigma^2) := \mathcal{N}(\mathbf{x}|\boldsymbol{\mu}, \sigma^2 I_d)$ to denote an isotropic normal distribution. Note that $dt < 0$ for inference, by definition. Furthermore, $\dot{\sigma}\sigma$ can be interpreted as diffusion coefficient, $\nabla_{\mathbf{x}} \log P(\mathbf{x}|\sigma^2)$ as score function, and $P(\mathbf{x}|\sigma^2) = \int_{\mathbb{R}^d} \mathcal{N}(\mathbf{x}|\mathbf{y}, \sigma^2)P(\mathbf{y})d\mathbf{y}$ as distribution of noisy samples, which results from adding Gaussian noise to data samples. To derive the optimal denoiser, we rewrite the score function as

$$\begin{aligned} -\nabla_{\mathbf{x}} \log P(\mathbf{x}|\sigma^2) &= -\frac{\nabla_{\mathbf{x}} P(\mathbf{x}|\sigma^2)}{P(\mathbf{x}|\sigma^2)} \\ &= -\frac{\nabla_{\mathbf{x}} \int_{\mathbb{R}^d} \mathcal{N}(\mathbf{x}|\mathbf{y}, \sigma^2)P(\mathbf{y})d\mathbf{y}}{P(\mathbf{x}|\sigma^2)} \\ &= \frac{\int_{\mathbb{R}^d} \frac{\mathbf{x}-\mathbf{y}}{\sigma^2} \mathcal{N}(\mathbf{x}|\mathbf{y}, \sigma^2)P(\mathbf{y})d\mathbf{y}}{P(\mathbf{x}|\sigma^2)} \\ &= \frac{1}{\sigma^2} \int_{\mathbb{R}^d} (\mathbf{x} - \mathbf{y})P(\mathbf{y}|\mathbf{x}, \sigma^2)d\mathbf{y} \\ &= \frac{1}{\sigma^2} \left(\int_{\mathbb{R}^d} \mathbf{x}P(\mathbf{y}|\mathbf{x}, \sigma^2)d\mathbf{y} - \int_{\mathbb{R}^d} \mathbf{y}P(\mathbf{y}|\mathbf{x}, \sigma^2)d\mathbf{y} \right) \\ &= \frac{\mathbf{x} - \mathbf{y}^*(\mathbf{x}, \sigma)}{\sigma^2}, \end{aligned} \quad (5)$$

where the optimal denoiser is given by the posterior mean

$$\mathbf{y}^*(\mathbf{x}, \sigma) := \int_{\mathbb{R}^d} \mathbf{y}P(\mathbf{y}|\mathbf{x}, \sigma^2)d\mathbf{y} = \int_{\mathbb{R}^d} \mathbf{y} \frac{\mathcal{N}(\mathbf{x}|\mathbf{y}, \sigma^2)P(\mathbf{y})}{P(\mathbf{x}|\sigma^2)} d\mathbf{y}. \quad (6)$$

To construct an error-prone denoiser, we substitute the true data distribution with a ‘‘broader’’ data distribution $P(\mathbf{y}) \rightarrow P_{\delta}(\mathbf{y})$, with $P_{\delta}(\mathbf{y}) = \int_{\mathbb{R}^d} \mathcal{N}(\mathbf{y}|\mathbf{y}', \delta^2)P(\mathbf{y}')d\mathbf{y}'$, where δ is the standard deviation of the noise that randomly shifts data points. The corresponding posterior mean is given by

$$\begin{aligned} \mathbf{y}_{\delta}(\mathbf{x}, \sigma) &:= \int_{\mathbb{R}^d} \mathbf{y} \frac{\mathcal{N}(\mathbf{x}|\mathbf{y}, \sigma^2)P_{\delta}(\mathbf{y})}{P_{\delta}(\mathbf{x}|\sigma^2)} d\mathbf{y} \\ &= \frac{\int_{\mathbb{R}^d} \int_{\mathbb{R}^d} \mathbf{y} \mathcal{N}(\mathbf{x}|\mathbf{y}, \sigma^2) \mathcal{N}(\mathbf{y}|\mathbf{y}', \delta^2) P(\mathbf{y}') d\mathbf{y}' d\mathbf{y}}{\int_{\mathbb{R}^d} \int_{\mathbb{R}^d} \mathcal{N}(\mathbf{x}|\mathbf{y}, \sigma^2) \mathcal{N}(\mathbf{y}|\mathbf{y}', \delta^2) P(\mathbf{y}') d\mathbf{y}' d\mathbf{y}}, \end{aligned} \quad (7)$$

with $P_{\delta}(\mathbf{x}|\sigma^2) := \int_{\mathbb{R}^d} \mathcal{N}(\mathbf{x}|\mathbf{y}, \sigma^2)P_{\delta}(\mathbf{y})d\mathbf{y}$. To find an explicit expression for \mathbf{y}_{δ} , we utilize known integrals [35]. For the denominator, we use the expression

$$\int_{\mathbb{R}^d} \phi(\mathbf{x})\phi(\mathbf{a} + b\mathbf{x})d\mathbf{x} = \frac{1}{\sqrt{1+b^2}}\phi\left(\frac{\mathbf{a}}{\sqrt{1+b^2}}\right). \quad (8)$$

with $\phi(\mathbf{x}) := \mathcal{N}(\mathbf{x}|0, 1)$. However, we have to reformulate this expression for the product of two Gaussians with different means and variances. To this end, consider the substitution $\mathbf{x} = \frac{\mathbf{z}-\mathbf{c}}{d}$, $c, d \in \mathbb{R}$ and adjust the LHS.

$$\begin{aligned} \int_{\mathbb{R}^d} \phi(\mathbf{x})\phi(\mathbf{a} + b\mathbf{x})d\mathbf{x} &= \int_{\mathbb{R}^d} \phi\left(\frac{\mathbf{z}-\mathbf{c}}{d}\right)\phi\left(\mathbf{a} + b\frac{\mathbf{z}-\mathbf{c}}{d}\right)\frac{1}{d}d\mathbf{z} \\ &= \int_{\mathbb{R}^d} \phi\left(\frac{\mathbf{z}-\mathbf{c}}{d}\right)\phi\left(\frac{\mathbf{z}-\boldsymbol{\mu}}{\sigma}\right)\frac{1}{d}d\mathbf{z} \quad , \quad \boldsymbol{\mu} = \mathbf{c} - \mathbf{a}\frac{d}{b}, \sigma = \frac{d}{b} \\ &= \sigma \int_{\mathbb{R}^d} \mathcal{N}(\mathbf{z}|\mathbf{c}, d^2)\mathcal{N}(\mathbf{z}|\boldsymbol{\mu}, \sigma^2)d\mathbf{z}. \end{aligned}$$

Combining with the RHS of Eq. (8) yields the desired integration formula

$$\begin{aligned}\int_{\mathbb{R}^d} \mathcal{N}(\mathbf{z}|\mathbf{c}, d^2)\mathcal{N}(\mathbf{z}|\boldsymbol{\mu}, \sigma^2)d\mathbf{z} &= \frac{1}{\sigma} \frac{1}{\sqrt{1+b^2}} \phi\left(\frac{\mathbf{a}}{\sqrt{1+b^2}}\right) \\ &= \frac{1}{\sqrt{\sigma^2+d^2}} \phi\left(\frac{\mathbf{c}-\boldsymbol{\mu}}{\sqrt{\sigma^2+d^2}}\right) = \mathcal{N}(\mathbf{c}|\boldsymbol{\mu}, \sigma^2+d^2).\end{aligned}\quad (9)$$

For the numerator, we use the expression [35]

$$\int_{\mathbb{R}^d} \mathbf{x}\phi(\mathbf{x})\phi(\mathbf{a}+b\mathbf{x})d\mathbf{x} = -\frac{ab}{(1+b^2)^{\frac{3}{2}}}\phi\left(\frac{\mathbf{a}}{\sqrt{1+b^2}}\right).\quad (10)$$

Using the same substitutions as before yields

$$\begin{aligned}\int_{\mathbb{R}^d} \mathbf{x}\phi(\mathbf{x})\phi(\mathbf{a}+b\mathbf{x})d\mathbf{x} &= \int_{\mathbb{R}^d} \frac{\mathbf{z}-\mathbf{c}}{d} \phi\left(\frac{\mathbf{z}-\mathbf{c}}{d}\right) \phi\left(\frac{\mathbf{z}-\boldsymbol{\mu}}{\sigma}\right) \frac{1}{d} d\mathbf{z} \\ &= \frac{1}{d} \int_{\mathbb{R}^d} \mathbf{z}\sigma\mathcal{N}(\mathbf{z}|\mathbf{c}, d^2)\mathcal{N}(\mathbf{z}|\boldsymbol{\mu}, \sigma^2)d\mathbf{z} - \frac{\mathbf{c}}{d} \int_{\mathbb{R}^d} \mathcal{N}(\mathbf{z}|\mathbf{c}, d^2)\mathcal{N}(\mathbf{z}|\boldsymbol{\mu}, \sigma^2)d\mathbf{z} \\ &\stackrel{(9)}{=} \frac{1}{d} \int_{\mathbb{R}^d} \mathbf{z}\sigma\mathcal{N}(\mathbf{z}|\mathbf{c}, d^2)\mathcal{N}(\mathbf{z}|\boldsymbol{\mu}, \sigma^2)d\mathbf{z} - \frac{\mathbf{c}}{d} \mathcal{N}(\mathbf{c}|\boldsymbol{\mu}, \sigma^2+d^2).\end{aligned}$$

Combining with the RHS of Eq. (10) yields the second integration formula

$$\begin{aligned}\int_{\mathbb{R}^d} \mathbf{z}\sigma\mathcal{N}(\mathbf{z}|\mathbf{c}, d^2)\mathcal{N}(\mathbf{z}|\boldsymbol{\mu}, \sigma^2)d\mathbf{z} &= \frac{d}{\sigma} \left(-\frac{\mathbf{c}-\boldsymbol{\mu}}{\sigma} \frac{d}{\sigma} \left(\frac{\sigma}{\sqrt{\sigma^2+d^2}} \right)^3 \phi\left(\frac{\mathbf{c}-\boldsymbol{\mu}}{\sqrt{\sigma^2+d^2}}\right) + \frac{\sigma\mathbf{c}}{d} \mathcal{N}(\mathbf{c}|\boldsymbol{\mu}, \sigma^2+d^2) \right) \\ &= \frac{d}{\sigma} \left(-\frac{(\mathbf{c}-\boldsymbol{\mu})d}{\sigma^2} \frac{\sigma^3}{\sigma^2+d^2} \mathcal{N}(\mathbf{c}|\boldsymbol{\mu}, \sigma^2+d^2) + \frac{\sigma\mathbf{c}}{d} \mathcal{N}(\mathbf{c}|\boldsymbol{\mu}, \sigma^2+d^2) \right) \\ &= \mathcal{N}(\mathbf{c}|\boldsymbol{\mu}, \sigma^2+d^2) \left(\mathbf{c} - \frac{(\mathbf{c}-\boldsymbol{\mu})d^2}{\sigma^2+d^2} \right) \\ &= \mathcal{N}(\mathbf{c}|\boldsymbol{\mu}, \sigma^2+d^2) \frac{\mathbf{c}\sigma^2 + \boldsymbol{\mu}d^2}{\sigma^2+d^2}.\end{aligned}\quad (11)$$

For the numerator, of Eq. (7) we now get

$$\begin{aligned}\int_{\mathbb{R}^d} \mathbf{y}\mathcal{N}(\mathbf{x}|\mathbf{y}, \sigma^2) \int_{\mathbb{R}^d} \mathcal{N}(\mathbf{y}|\mathbf{y}', \delta^2)P(\mathbf{y}')d\mathbf{y}'d\mathbf{y} &= \int_{\mathbb{R}^d} \int_{\mathbb{R}^d} \mathbf{y}\mathcal{N}(\mathbf{y}|\mathbf{x}, \sigma^2)\mathcal{N}(\mathbf{y}|\mathbf{y}', \delta^2)d\mathbf{y}P(\mathbf{y}')d\mathbf{y}' \\ &\stackrel{(11)}{=} \int_{\mathbb{R}^d} \mathcal{N}(\mathbf{x}|\mathbf{y}', \sigma^2+\delta^2) \frac{\mathbf{x}\delta^2 + \mathbf{y}'\sigma^2}{\sigma^2+\delta^2} P(\mathbf{y}')d\mathbf{y}' \\ &= \frac{1}{\sigma^2+\delta^2} \int_{\mathbb{R}^d} (\mathbf{x}\delta^2 + \mathbf{y}'\sigma^2)P(\mathbf{x}, \mathbf{y}'|\sigma^2+\delta^2)d\mathbf{y}'.\end{aligned}\quad (12)$$

For the denominator of Eq. (7), we now get

$$\begin{aligned}P_\delta(\mathbf{x}|\sigma^2) &= \int_{\mathbb{R}^d} \mathcal{N}(\mathbf{x}|\mathbf{y}, \sigma^2)P_\delta(\mathbf{y})d\mathbf{y} \\ &= \int_{\mathbb{R}^d} \mathcal{N}(\mathbf{x}|\mathbf{y}, \sigma^2) \int_{\mathbb{R}^d} \mathcal{N}(\mathbf{y}|\mathbf{y}', \delta^2)P(\mathbf{y}')d\mathbf{y}'d\mathbf{y} \\ &= \int_{\mathbb{R}^d} \int_{\mathbb{R}^d} \mathcal{N}(\mathbf{y}|\mathbf{x}, \sigma^2)\mathcal{N}(\mathbf{y}|\mathbf{y}', \delta^2)d\mathbf{y}P(\mathbf{y}')d\mathbf{y}' \\ &\stackrel{(9)}{=} \int_{\mathbb{R}^d} \mathcal{N}(\mathbf{x}|\mathbf{y}', \sigma^2+\delta^2)P(\mathbf{y}')d\mathbf{y}' \\ &= \int_{\mathbb{R}^d} \mathcal{N}(\mathbf{x}|\mathbf{y}', \sigma^2+\delta^2)P(\mathbf{y}')d\mathbf{y}' \\ &= P(\mathbf{x}|\sigma^2+\delta^2).\end{aligned}\quad (13)$$

Finally,

$$\begin{aligned}
\mathbf{y}_\delta(\mathbf{x}, \sigma) &\stackrel{(12)+(13)}{=} \frac{\int_{\mathbb{R}^d} (\mathbf{x}\delta^2 + \mathbf{y}'\sigma^2) P(\mathbf{x}, \mathbf{y}'|\tilde{\sigma}^2) d\mathbf{y}'}{P(\mathbf{x}|\tilde{\sigma}^2)} \frac{1}{\tilde{\sigma}^2} \\
&= \frac{\mathbf{x}\delta^2 \int_{\mathbb{R}^d} P(\mathbf{x}, \mathbf{y}'|\tilde{\sigma}^2) d\mathbf{y}' + \sigma^2 \int_{\mathbb{R}^d} \mathbf{y}' P(\mathbf{x}, \mathbf{y}'|\tilde{\sigma}^2) d\mathbf{y}'}{P(\mathbf{x}|\tilde{\sigma}^2)} \frac{1}{\tilde{\sigma}^2} \\
&= \frac{\mathbf{x}\delta^2 + \sigma^2 \int_{\mathbb{R}^d} \mathbf{y}' \frac{P(\mathbf{x}, \mathbf{y}'|\tilde{\sigma}^2)}{P(\mathbf{x}|\tilde{\sigma}^2)} d\mathbf{y}'}{\tilde{\sigma}^2} \\
&= \frac{\mathbf{x}\delta^2 + \mathbf{y}^*(\mathbf{x}, \tilde{\sigma})\sigma^2}{\tilde{\sigma}^2}.
\end{aligned} \tag{14}$$

with $\tilde{\sigma}^2 = \sigma^2 + \delta^2$. Using optimal denoiser \mathbf{y}^* , we can define the optimal noise predictor

$$\boldsymbol{\epsilon}^*(\mathbf{x}, t) := \frac{\mathbf{x} - \mathbf{y}^*(\mathbf{x}, \sigma)}{\sigma} \stackrel{(5)}{=} \sigma \nabla_{\mathbf{x}} \log P(\mathbf{x}|\sigma^2) \tag{15}$$

and similarly, we define the error-prone noise predictor by

$$\boldsymbol{\epsilon}_{err}(\mathbf{x}, t) := \frac{\mathbf{x} - \mathbf{y}_\delta(\mathbf{x}, \sigma)}{\sigma}. \tag{16}$$

Inserting the explicit expression for \mathbf{y}_δ in Eq. (16) yields the expression for $\boldsymbol{\epsilon}_{err}$ used in the main text

$$\boldsymbol{\epsilon}_{err}(\mathbf{x}, \sigma) = \frac{\mathbf{x} - \mathbf{y}_\delta(\mathbf{x}, \sigma)}{\sigma} = \frac{\mathbf{x} - \frac{\mathbf{x}\delta^2 + \mathbf{y}^*(\mathbf{x}, \tilde{\sigma})\sigma^2}{\tilde{\sigma}^2}}{\sigma} = \frac{1}{\sigma} \frac{\sigma^2(\mathbf{x} - \mathbf{y}^*(\mathbf{x}, \tilde{\sigma}))}{\tilde{\sigma}^2} = \frac{\sigma^2}{\tilde{\sigma}^2} \boldsymbol{\epsilon}^*(\mathbf{x}, \tilde{\sigma}).$$

We can now generate trajectories $\mathbf{x}(t)$ from Eq. (4) by numerically solving the ODE with \mathbf{y}^* or \mathbf{y}_δ , corresponding to $\boldsymbol{\epsilon}^*$ or $\boldsymbol{\epsilon}_{err}$. In practice, we consider a finite set of data-points $\{\mathbf{y}_i\}_{i=1}^N$, in which case Eq. (6) and Eq. (14) simplify to

$$\mathbf{y}^*(\mathbf{x}, \sigma) = \frac{\sum_i \mathbf{y}_i N(\mathbf{x}(t)|\mathbf{y}_i, \sigma^2)}{\sum_i N(\mathbf{x}(t)|\mathbf{y}_i, \sigma^2)} \tag{17}$$

$$\mathbf{y}_\delta(\mathbf{x}, \sigma) = \frac{\mathbf{x}\delta^2 + \mathbf{y}^*(\mathbf{x}, \tilde{\sigma})\sigma^2}{\tilde{\sigma}^2}, \tag{18}$$

which can be directly used to simulate trajectories. To do so, we use the Euler method shown in Algorithm 1. We found that higher-order integration methods (e.g., Alg. 1 of Ref. [24]) can be used but are not necessary to achieve sufficient accuracy. This framework can be used for simulations of different configurations of $\boldsymbol{\epsilon}^*$, $\boldsymbol{\epsilon}_{err}$, conditional and unconditional models, as well as arbitrary finite datasets in \mathbb{R}^2 . Figs. 18 and 19 show a detailed analysis of WMG on two datasets, the triangle formation used in the main text and a cloud of normally distributed data samples.

Algorithm 1 Euler method

Require: positive denoiser \mathbf{y}_δ , negative denoiser $\mathbf{y}_{\delta'}$, guidance weight $w(\mathbf{x}, \sigma)$, $t_i \in \{0, \dots, N\} \in [0, 1]$

sample $x_0 \sim \mathcal{N}(\mathbf{x}|0, \sigma(1)^2 I_d)$

for i in $0, \dots, N - 1$ **do**

$\sigma_i, \sigma_{i+1} = \sigma(t_i), \sigma(t_{i+1})$

$\tilde{\mathbf{y}}_i = \mathbf{y}_\delta(\mathbf{x}_i, \sigma_i^2) + w(\mathbf{x}, \sigma_i)[\mathbf{y}_\delta(\mathbf{x}_i, \sigma_i^2) - \mathbf{y}_{\delta'}(\mathbf{x}_i, \sigma_i^2)]$

$\mathbf{d}_i = (\mathbf{x}_i - \tilde{\mathbf{y}}_i)/\sigma_i$

$\mathbf{x}_{i+1} = \mathbf{x}_i + (\sigma_{i+1} - \sigma_i)\mathbf{d}_i$

▷ Set current and next noise level

▷ Compute guidance target prediction

▷ Compute score

▷ Update the trajectory

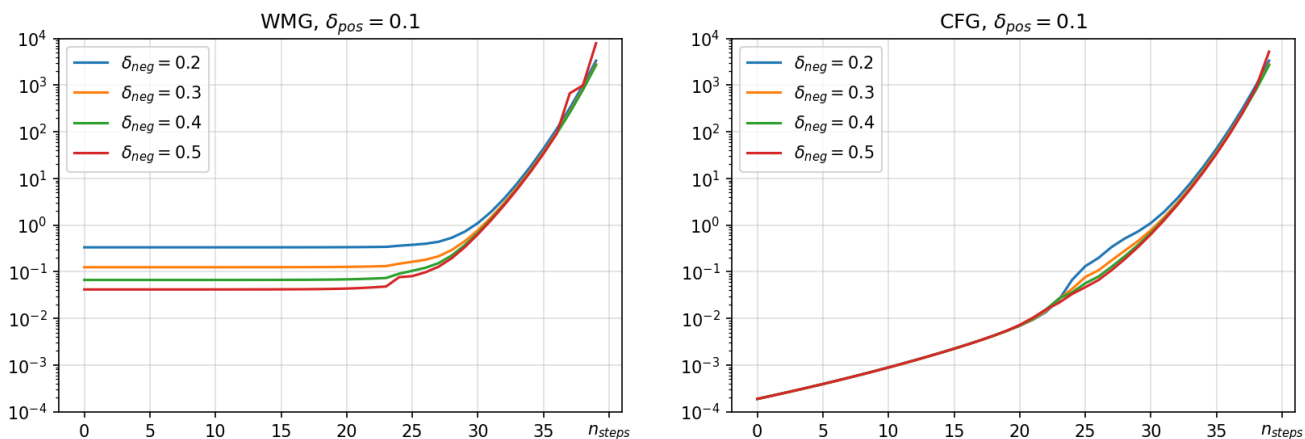


Figure 17. Optimal guidance weight for WMG and CFG in a toy example simulation. The x -axis shows number of sampling steps and the y -axis the guidance weight value, averaged over 100 trajectories with random initialization. The dataset and models ϵ_{pos} and ϵ_{neg} are as described in the main text. For both guidance methods, ϵ_{pos} has a variance of $\delta_{\text{pos}} = 0.1$ and different values for δ_{neg} are shown.

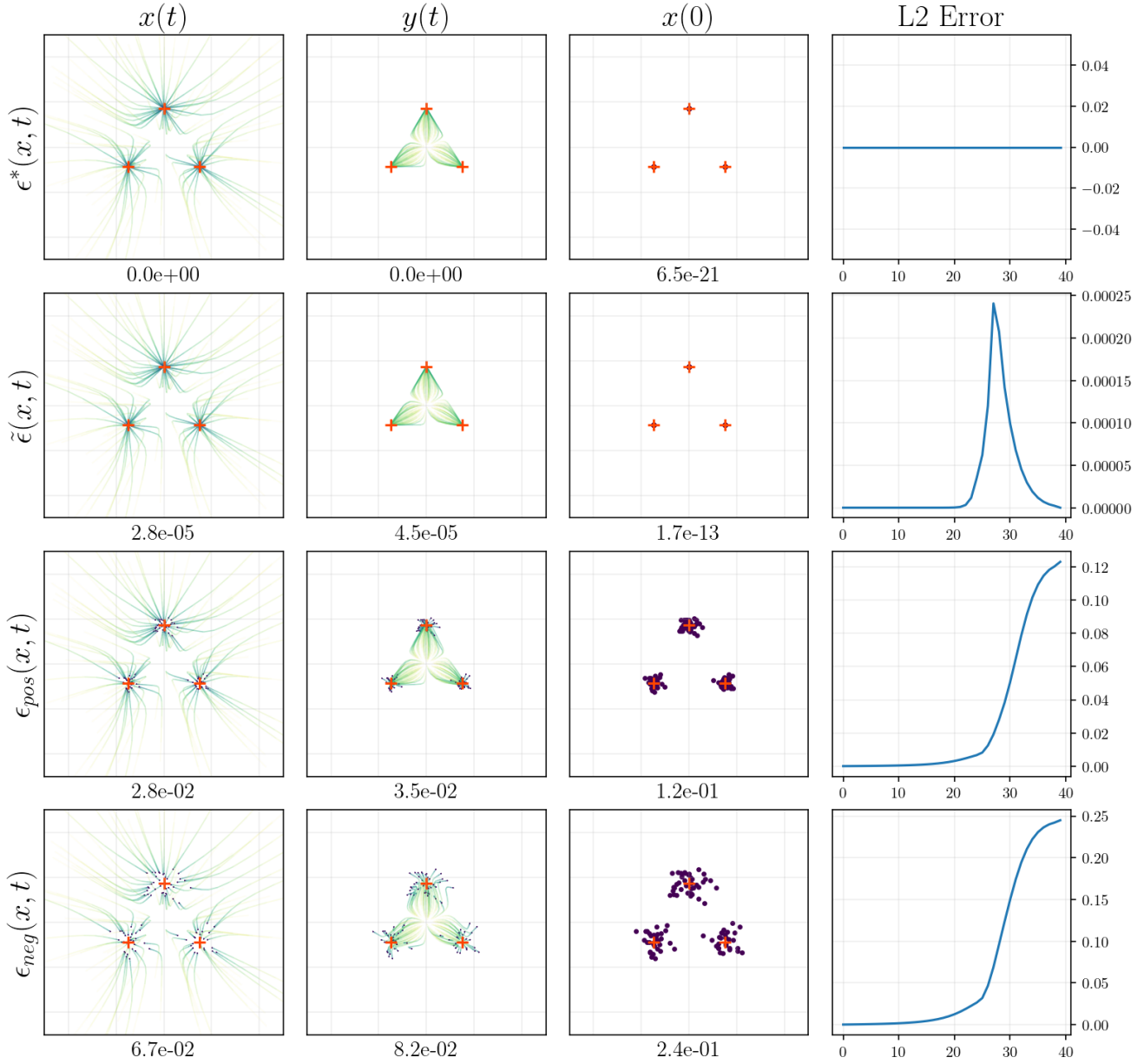


Figure 18. Full toy example simulation for WMG with optimal guidance weight $w^*(\mathbf{x}, t)$ and 40 sampling steps. Columns show the trajectory $\mathbf{x}(t)$, the target prediction $\mathbf{y}(t)$, the trajectory endpoints $\mathbf{x}(T)$, and the average step-wise L2 error to the optimal noise predictor ϵ^* along the trajectory. The numbers below the plots in the first three columns show the average L2 error to the optimal trajectory (additionally averaged over steps for $\mathbf{x}(t)$ and $\mathbf{y}(t)$). Rows show the optimal noise predictor ϵ^* , the WMG noise predictor $\tilde{\epsilon} = \epsilon_{pos} + w[\epsilon_{pos} - \epsilon_{neg}]$ with optimal weight $w^*(\mathbf{x}, t)$, ϵ_{pos} ($w = 0$), and ϵ_{neg} ($w = -1$).

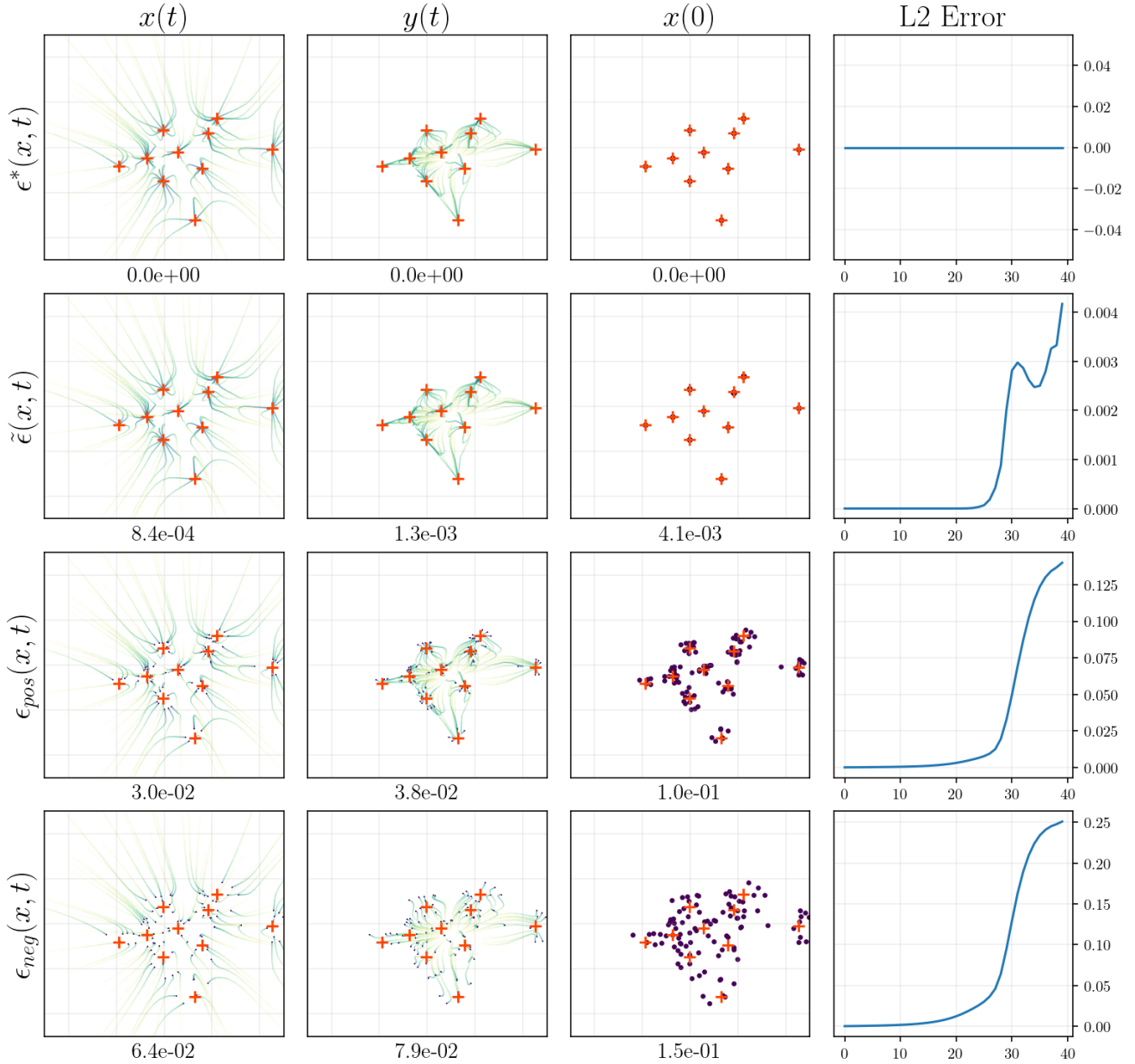


Figure 19. Full toy example simulation for WMG with optimal guidance weight $w^*(x, t)$, a cloud of normally distributed data points, and 40 sampling steps. Columns show the trajectory $x(t)$, the target prediction $y(t)$, the trajectory endpoints $x(T)$, and the average step-wise L2 error to the optimal noise predictor ϵ^* along the trajectory. The numbers below the plots in the first three columns show the average L2 error to the optimal trajectory (additionally averaged over steps for $x(t)$ and $y(t)$). Rows show the optimal noise predictor ϵ^* , the WMG noise predictor $\tilde{\epsilon} = \epsilon_{pos} + w[\epsilon_{pos} - \epsilon_{neg}]$ with optimal weight $w^*(x, t)$, ϵ_{pos} ($w = 0$), and ϵ_{neg} ($w = -1$).